Toward an Understanding of the Retinal Chromophore in Rhodopsin Mimics

11 AUTHORS, INCLUDING:

Mikas Vengris
Vilnius University
64 PUBLICATIONS **1,182** CITATIONS

SEE PROFILE

James H Geiger
Michigan State University
71 PUBLICATIONS **2,370** CITATIONS

SEE PROFILE

Delmar S Larsen
University of California, Davis
86 PUBLICATIONS **2,700** CITATIONS

SEE PROFILE

Toward an Understanding of the Retinal Chromophore in Rhodopsin Mimics

Mark M. Huntress,[†] Samer Gozem,[†] Konstantin R. Malley,[‡] Askat E. Jailaubekov,[‡] Chrysoula Vasileiou,[§] Mikas Vengris,[‡,‖] James H. Geiger,[§] Babak Borhan,[§] Igor Schapiro,[†] Delmar S. Larsen,*[‡] and Massimo Olivucci*[†]

[†]Department of Chemistry, Bowling Green State University, Bowling Green, Ohio 43402, United States
[‡]Department of Chemistry, University of California Davis, One Shields Avenure, Davis, California 95616, United States
[§]Department of Chemistry, Michigan State University, Lansing, Michigan 48824, United States
[‖]Faculty of Physics, Vilnius University, Sauletekio 10 LT10223 Vilnius, Lithuania

S *Supporting Information*

ABSTRACT: Recently, a rhodopsin protein mimic was constructed by combining mutants of the cellular retinoic acid binding protein II (CRABPII) with an all-trans retinal chromophore. Here, we present a combined computational quantum mechanics/molecular mechanics (QM/MM) and experimental ultrafast kinetic study of CRABPII. We employ the QM/MM models to study the absorption (λ^a_{max}), fluorescence (λ^f_{max}), and reactivity of a CRABPII triple mutant incorporating the all-trans protonated chromophore (PSB-KLE-CRABPII). We also study the spectroscopy of the same mutant incorporating the unprotonated chromophore and of another double mutant incorporating the neutral unbound retinal molecule held inside the pocket. Finally, for PSB-KLE-CRABPII, stationary fluorescence spectroscopy and ultrafast transient absorption spectroscopy resolved two different evolving excited state populations which were computationally assigned to distinct locally excited and charge-transfer species. This last species is shown to evolve along reaction paths describing a facile isomerization of the biologically relevant 11-cis and 13-cis double bonds. This work represents a first exploratory attempt to model and study these artificial protein systems. It also indicates directions for improving the QM/MM models so that they could be more effectively used to assist the bottom-up design of genetically encodable probes and actuators employing the retinal chromophore.
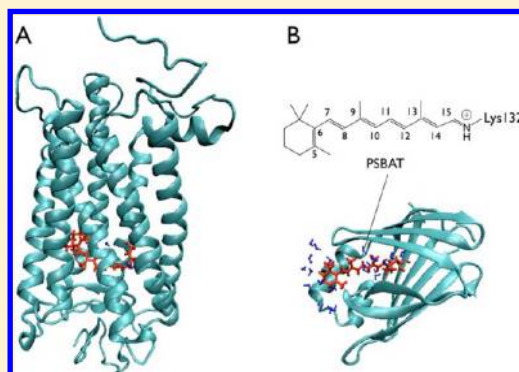
1. INTRODUCTION

Rhodopsins comprise a family of light-absorbing proteins that have sensory and ion-pumping functions in a wide range of organisms.[1,2] Rhodopsins feature an α-helical transmembrane structure (Figure 1A) hosting a retinal chromophore which remains isolated from the solvent in a protein pocket.[3] The chromophore in such rhodopsins can normally be found in the 11-*cis* (in visual pigments), 13-*cis* (in microbial pigments), or all-*trans* conformation (in both visual and microbial pigments) and is covalently connected to a lysine residue via a protonated Schiff base linkage. The interaction of the chromophore with diverse protein environments induces a wide range of absorption maxima (λ^a_{max}) ranging from 350 to 630 nm.[4,5] A significant amount of this λ^a_{max} determination (i.e., color tuning) results from changes in the chromophore binding pocket (i.e., the environment around the chromophore), although more extreme shifts can be induced by manipulating the protonation of the Schiff base linkage,[6] or by chemical modifications of the chromophore[7,8] (for instance, one which causes it to be held in an unbound state as a neutral retinal molecule).[9]

The protein environment not only tunes the λ^a_{max} of the chromophore but also influences the chromophore excited state dynamics, quantum yield, and reaction selectivity.[10] For example, in solution, the protonated all-*trans* retinal Schiff base (PSBAT) photoisomerizes about both the C11═C12 and C13═C14 double bonds and, to a lesser extent, around the C9═C10 double bond,[11,12] while in bacterial pigments such as bacteriorhodopsin (bR) and *anabaena* sensory rhodopsin (ASR) the photoisomerization is selective, leading to the 13-*cis* form (PSB13) exclusively.[13−16] Similarly, bovine rhodopsin (Rh) photoisomerization transforms its 11-*cis* chromophore (PSB11) to PSBAT exclusively. The differences between protein and solution environments also modulate the excited state dynamics. Indeed, in Rh and bR, the excited state is rapidly quenched within the first ~200 and ~500 fs, respectively.[14,17] In contrast, PSBAT and PSB13 in solution
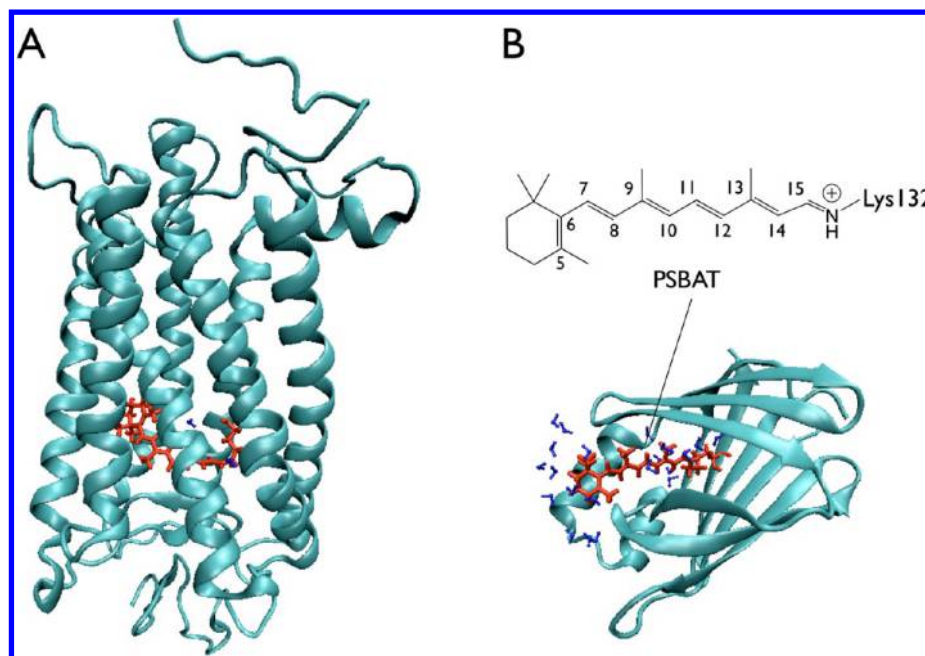
Figure 1. (A) Crystal structure of Rh (Protein Data Bank record 1U19, chain A). The 11-*cis* retinal chromophore (displayed in red) is buried in the binding pocket of the protein. (B) The all-*trans* protonated retinal Schiff base (PSBAT) linkage and the crystal structure of the KLE mutant of CRABPII (Protein Data Bank record 2G7B) binding a PSBAT chromophore (displayed in red). The structure is dominated by beta sheets forming a barrel shape, with a helix-turn-helix motif at the entrance to the binding pocket. The chromophore is partially exposed to solvent (displayed in blue).

exhibit appreciably slower (∼3 ps) excited state quenching kinetics.[18,19]

The engineering of proteins that spontaneously acquire chromophores and that exhibit desired colorimetric, fluorescent, and photochromic properties is revolutionizing the observation of cellular states.[10,20−26] While rhodopsins are not currently regarded as cornerstones for the development of optical probes, they absorb a wide range of colors and some have exhibited photochromic behavior, as has been documented for channelrhodopsin,[27,28] octopus rhodopsin,[29] ASR,[30,31] and different bR mutants.[32,33] Furthermore, a weak fluorescence has been demonstrated in a modified Rh incorporating an artificial 11-*cis* locked chromophore.[34,35] In the same vein, Cohen and co-workers have recently reported two rhodopsin-based voltage-sensitive fluorescent proteins: the proteorhodopsin optical proton sensor[36] and archaerhodopsin 3.[37] Overall, these findings suggest that the incorporation of a retinal chromophore in suitably engineered protein environments may result in novel, genetically encodable, optical probes. In fact, studies have already begun to emerge toward this aim.[38,39]

Although nature has been fine-tuning protein activity for millions of years, the engineering of artificial proteins with desired functions is still in its infancy. Often, researchers follow a top-down or "reverse engineering" approach for deciphering how complex protein−chromophore interactions dictate function, whereby protein complexes are studied by investigating the effects of small changes to the structure on activity or function. This is typically accomplished by introducing point mutations,[40,41] incorporating modified non-native cofactors into either a native[42] or modified[43] cofactor binding site, or larger scale modifications of the protein backbone[44] such as transforming a tetramer into a dimer or monomer.[45] Alternative bottom-up (i.e., "positive engineering" or "rational design") approaches use knowledge obtained from top-down studies to develop novel environments from known or predictable three-dimensional scaffolding.[46−49]

Recently, Borhan and co-workers used a bottom-up approach to re-engineer the cellular retinoic acid binding protein II (CRABPII) into a rhodopsin protein mimic.[50,51] CRABPII is a protein that exists in water solution in the cytosol and noncovalently binds all-*trans* retinoic acid[52] to regulate its cellular concentration and to solubilize and protect it from isomerization.[53−55] With a very similar structure to retinoic acid, all-*trans* retinal fits well into the same binding pocket, and after a small number of specific mutations, it covalently binds to the CRABPII protein scaffolding. In particular, the R132K:R111L:L121E (KLE) triple mutant spontaneously incorporates a PSBAT chromophore (Figure 1B) bound to K132 via a protonated Schiff base linkage that is stabilized by a salt-bridge with the ionized E121 residue.[56] The result is a retinal binding protein (PSB-KLE-CRABPII) that mimics natural rhodopsins but has a radically different structure and exhibits different spectroscopic properties. A comparison between KLE-CRABPII (Figure 1B) and a prototypal natural rhodopsin, Rh (Figure 1A), reveals that KLE-CRABPII is considerably smaller (137 instead of 348 residues) with a chromophore pocket that is surrounded by a β-strand rather than α-helix segments. Moreover, the chromophore in KLE-CRABPII is exposed to solvent, since the protein hosts many water molecules as opposed to Rh which has only two, as indicated by the 1U19 crystal structure,[3] or three, as suggested by Bravaya et al.[57] The pocket has a limited depth, so when retinal binds to KLE-CRABPII, its β-ionone ring protrudes out to the protein surface (Figure 1B). Also, the chromophore in KLE-CRABPII is PSBAT, while Rh binds PSB11. The differences in these protein environments result in a blue-shift of the PSB-KLE-CRABPII λ^a_{max} (449 nm)[51] relative to Rh (498 nm).[58]

CRABPII-based rhodopsin mimics can be easily engineered and crystallized, and are amenable to transient spectroscopies. Since crystal structures of natural rhodopsins cannot be routinely obtained due to difficulties in generating suitably diffracting crystals, these mimics provide ideal "laboratory" systems for investigating the possibility of engineering new PSBAT based fluorescent proteins. In fact, their crystal structure allows for the construction of quantum mechanics/molecular mechanics (QM/MM) models[59] of CRABPII mutants that can be used to guide rational design approaches.

To engineer rhodopsin mimics into functioning probes, the availability of modeling strategies capable of assisting the search for mutants with desired λ^a_{max} or λ^f_{max} values and photochemical reactivity (Figure 2) is highly desirable. For this
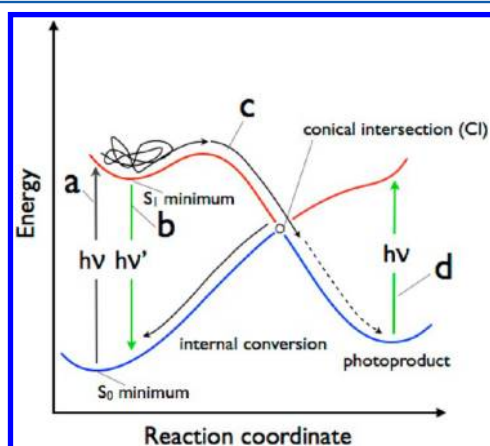
Figure 2. The light-induced processes modeled in this work. The first process (a) corresponds to light absorption and is responsible for the color of the rhodopsin mimics. The second process (b) corresponds to light emission (fluorescence) and can be modeled by looking for excited state energy minima. Process c corresponds to the excited state isomerization of the retinal chromophore, leading to quenching via a conical intersection channel and nonunity formation (part of the reacting population can revert back to the original reactant, leading to internal conversion) of photoproduct, whose absorption corresponds to process d.

reason, below we present a combined computational QM/MM and ultrafast kinetic experimental study of a CRABPII system representing a first step toward the exploration of the photophysics of these new protein systems. Note that this is a first exploratory and, possibly, crude attempt to model and study these engineered proteins, paving the way for future systematic studies of such systems. In particular, here we investigate three systems for which experimental data is available: the aforementioned PSB-KLE-CRABPII protein, the corresponding form (SB-KLE-CRABPII) hosting the unprotonated form of PSBAT (SBAT), and the KF-CRABPII (R132K:Y134F) mutant with an unbound retinal molecule held in the binding pocket. The results are contrasted with those of analogue studies of solvated PSBAT and Rh. We employ QM/MM models of these systems in an attempt to reproduce the observed λ^a_{max} value (process a in Figure 2) of PSB-KLE-CRABPII, SB-KLE-CRABPII, and KF-CRABPII. We also explore the chromophore fluorescence (process b in Figure 2) in PSB-KLE-CRABPII, for which faint fluorescence was experimentally observed. Complementary time-resolved absorption spectroscopy and excited state QM/MM scans provide information about the PSB-KLE-CRABPII photoisomerization

mechanism/dynamics and photoproduct generation (processes c and d in Figure 2, respectively).

2. METHODS

2.1. Computations. Protein models capable of addressing diverse processes such as light-absorption, light-emission, and photoisomerization require quantum chemical methods capable of describing both ground and electronically excited states of the chromophore with comparable accuracy. The *ab initio* complete-active-space self-consistent-field (CASSCF) method is a multiconfigurational method offering enough flexibility for an unbiased description (i.e., with no empirically derived parameters and with multideterminant wave functions) of the electronic and equilibrium structures of the ground and excited states. Furthermore, the CASSCF wave function can be used for subsequent single-state and multistate multiconfigurational second-order perturbation theory (CASPT2[60] and MS-CASPT2,[61] respectively) computations to account for dynamic electron correlation when evaluating the energy gap between different electronic states or the energy barrier found for a given state. In this protocol, energies and equilibrium structures are determined at the CASPT2 and CASSCF levels of theory, respectively (we use the notation CASPT2//CASSCF), and using the 6-31G* basis set. It has been shown that a CASPT2//CASSCF based QM/MM protocol allows one to reproduce the λ^a_{max} of different proteins incorporating cationic, anionic, and neutral chromophores.[62−69] For visual and sensory rhodopsins, the excitation energies associated with the experimentally observed λ^a_{max} values have been reproduced with a root-mean-square error of ∼3 kcal/mol.[31,64,67,70−74] However, it has to be pointed out that these rhodopsins are less complex and less configurationally flexible than the artificial systems modeled in the present work. Therefore, the same type of QM/MM model may not display similar performances. Indeed, the evaluation of the applicability of such models to rhodopsin mimics is among the targets of the present work. However, although similar QM/MM studies on natural rhodopsins have been carried out with different quantum chemical protocols,[75,76] CASPT2//CASSCF is a practical method for a consistent description of spectra, reaction paths, conical intersections, and trajectories.[66,77−79] Furthermore, the error associated with such a method has been recently examined. When using CASSCF equilibrium structures, CASPT2 (with IPEA = 0) and a double-ζ basis set with polarization function computed energy gaps are comparable to experiment. The technical reason, ascribed to a balanced error cancelation,[80] has also been investigated quantitatively in a recent contribution.[81] Moreover, it has also been shown that CASSCF equilibrium geometries optimized in a protein environment may be closer to the correct geometry than when optimized in the gas phase.[82,83]

The QM/MM models (see sections 1.a, 1.b, and 1.e in the Supporting Information for details) of the CRABPII constructs were built on the basis of heavy atom coordinates from known crystal structures from the Protein Data Bank (2G79 and 2G7B) of 1.69 and 1.18 Å resolution, respectively.[51] After addition and MM minimization of hydrogens, the protein was placed in a 10 Å by 10 Å solvent box of water, and all the hydrogens of the water molecules were optimized. Next, a 1 ns molecular dynamics (MD) simulation was carried out at the MM level with the NAMD software[84] and AMBER parameters[85] to sample the internal water orientations and to account for the fluctuations in the hydrogen bond network (HBN). The waters were unconstrained, but the protein and

chromophore atoms (with the exception of the E121 counterion side chain) were held fixed at their crystal structure positions during the MD. Ten geometries were sampled from the last 200 ps of the trajectory and were used for QM/MM geometry optimization at the CASSCF/AMBER level (with an active space of 12 electrons in 12 orbitals spanning the entire π-system of the chromophore) to generate a set of models suitable for subsequent CASPT2//CASSCF/AMBER calculations. All QM/MM calculations were performed using Molcas 7.5[86] and utilized electrostatic embedding with a hydrogen link atom at the truncated C—C bond of the QM/MM boundary. The QM segment included the chromophore, the C_ξ and N of the lysine side chain, and hydrogens attached to these two atoms. The chromophore, counterion side chain, and proximal waters within 5 Å of the chromophore were optimized. The rest of the protein was kept frozen during the optimization. Therefore, we make the assumption that the high-resolution crystal structure provides an acceptable average representation of the protein backbone and side-chain structures. The λ^a_{max} was evaluated using three-root MS-CASPT2 calculations to alleviate the state mixing problems that were observed at the CASPT2 level between S_1 and S_2. Due to possible artifacts arising in CASPT2 and MS-CASPT2 near degeneracies,[81,87] a discussion of this point is reported in section 1.i of the Supporting Information where MS-CASPT2 and CASPT2 energies are compared to XMCQDPT2 energies. XMCQDPT2 is an extended multiconfigurational quasi-degenerate second order perturbation theory implemented in the Firefly quantum chemistry package.[88] The light emission and evolution on the excited state potential energy surface were explored at the CASPT2 rather than the MS-CASPT2 level, as only weak state mixing was observed in these cases.

The resulting PSB-KLE-CRABPII, SB-KLE-CRABPII, and KF-CRABPII models used in this study were compared to those of (1) a Rh model[67] built using the same protocol to serve as a reference and starting from the 1U19 crystal structure (see section 1.g in the Supporting Information),[3] (2) a model of PSBAT in water (see section 1.h in the Supporting Information), (3) two point mutants (A36D and A36H) of PSB-KLE-CRABPII that were created *in silico* to investigate the effect of introducing a negative and a positive charge near the poorly solvated region of the chromophore (see section 1.f in the Supporting Information). To account for the change in protein structure from the mutations, all side chains within 4.0 Å of A36 were optimized for each protein system.

All protein models are constructed with a substantially consistent, although approximated, protocol to allow for comparison. Of course, it was necessary to make some assumptions regarding the protonation state of E181 in Rh (see section 1.g of the Supporting Information) and to assume that the CASPT2//CASSCF/6-31G* method provides an adequate quantum chemistry level for the present exploratory investigation. On the other hand, even reasonably well reproduced quantities, such as λ^a_{max} and λ^f_{max} values, obtained with the employed level have been reported to rely on error cancellation effects, as shown for a gas-phase minimal model of the retinal chromophore.[81]

To investigate the internal conversion and photoisomerization mechanisms of PSB-KLE-CRABPII, we computed relaxed scans along its excited state potential energy surface to get information on the reaction path structure. Because the isomerization could occur along different bonds (either C10—C11=C12—C13 or C12—C13=C14—C15), and

could also occur along different directions (clockwise or counterclockwise due to the chirality of the protein environment), we computed four scans (in each direction along both the C10—C11=C12—C13 and C12—C13=C14—C15 dihedrals). The scans were generated at the CASPT2//CASSCF/AMBER level, consistent with similar scans reported for Rh models[74] (CASPT2 is more reliable than MS-CASPT2 in the absence of state mixing).[57,89−96] As the chromophore twists, the state mixing is reduced due to the divergence of the S_1 and S_2 energies (see Figure S8 and section 4.a of the Supporting Information). The scans are defined by 10° steps in the C10—C11=C12—C13 and C12—C13=C14—C15 dihedral angles of the PSBAT chromophore to track the corresponding isomerization mechanisms.

In order to reinforce the conclusions of the PSB-KLE-CRABPII excited state mapping, we also present gas-phase calculations of a reduced model of PSBAT (PSB3 in the following) featuring three conjugated double bonds: $C5H_2$=C4H—C3H=C2H—C1H=NH_2(+). Owing to the reduced size of this system, both energy evaluations and geometry optimizations were carried out at the two-root state-average CASPT2/6-31G* level with an IPEA shift of 0.00 and an imaginary shift of 0.2. The employed active space comprises six electrons in the six orbitals spanning the PSB3 π-system. Relaxed scans were performed along the C3=C2—C1=N dihedral (describing the twisting about a single bond) by constraining the dihedral value at several progressing values, and also constraining the H—C2—C1—H dihedral value in order to avoid pyramidalization. A second relaxed scan was computed with the same modalities following the double bond isomerization coordinate around the central C4—C3=C2—C1 dihedral. Any excited state minimum or maximum found along the scan was then optimized with no constraints.

2.2. Static and Transient Spectroscopic Measurements. Static fluorescence spectra were recorded with a Fluorolog-3 fluorometer (Instruments S. A., Inc.). All-*trans* retinal was purchased from Toronto Research Chemicals and was used as received. The emission spectrum of a 3 mL solution of the KLE-CRABII mutant in phosphate buffered saline (5 μM, pH 7.3) was recorded (λ_{ex} = 440 nm, spectrum range: 470−800 nm). One equivalent of all-*trans* retinal was added (3 μL of a 5 mM all-*trans* retinal solution in ethanol), the solution was mixed, and the emission spectrum was recorded. The PSB-KLE-CRABII protein−retinal complex was also recorded on the same instrument.

The full details of the experimental setup for the transient absorption signals have been described elsewhere.[97] Briefly, the 400 nm pump pulse was generated by the frequency doubling of the fundamental 800 nm output of a Ti:sapphire laser system (Spectra Physics Tsunami and Spitfire Pro) in a β-barium borate crystal to produce 2 μJ pulses of 50 fs duration at the 400 nm excitation wavelength. The probe pulse was produced by passing a 1 μJ portion of the 800 nm fundamental beam through a slowly translating 2 mm thick CaF_2 crystal to generate the broadband white light continuum used for probing. The pump beam was linearly polarized at the magic angle (54.7°) with respect to the probe beam to avoid reorientation effects from contributing to the signals. Samples were flowed through a custom-built cuvette constructed with 150 μm thick SiO_2 windows to reduce interfering cross-phase modulation artifacts[98,99] and to improve the time resolution by reducing pump−probe walk off. A peristaltic pump (Watson Marlow 401U/D) was used to flow the sample at a sufficient

speed to ensure replenishment of new sample between successive laser shots (1 ms). The absorbance of the samples was set to approximately 0.8 at the 800 μm path length of the cuvette.

PSBAT samples were prepared from all-*trans* retinal (Sigma) and *n*-butylamine (Aldrich) according to previously described methods.[100] A molar excess of *n*-butylamine was added to an 11 mM solution of all-*trans* retinal in anhydrous diethyl ether. The mixture was allowed to react for 24 h over 3 Å molecular sieves to absorb the water produced from condensation. The solvent was then evaporated under reduced pressure, and the sample was washed with diethyl ether three to four times to remove unreacted amine. After redissolving the sample in methanol, it was subsequently protonated with an excess of HCl to generate PSBAT, which is analogous to the linkage between a Lys residue and the retinal chromophore in Rh and bR.[101] The free unprotonated SBAT in methanol absorbs at 364 nm and shifts to 445 nm upon protonation.

The protocol, regarding CRABPII proteins, for binding all-*trans* retinal to the Lys132 residue of KLE-CRABPII as PSBAT, and the static spectroscopic properties of the PSB-KLE-CRABPII have been described previously.[50,51] The PSB-KLE-CRABPII sample was suspended in a phosphate buffered saline solution of pH 7.4 and adjusted dropwise with 0.2 M HCl to pH 7.2 to ensure that the Schiff base was fully protonated as determined spectroscopically. The static absorption spectra of the samples measured before and after laser excitation exhibit no significant change in shape or amplitude.

3. RESULTS AND DISCUSSION

3.1. Femtosecond Transient Dynamics. The femtosecond transient spectra for PSB-KLE-CRABPII are contrasted with PSBAT in methanol in Figure 3. The PSBAT signals
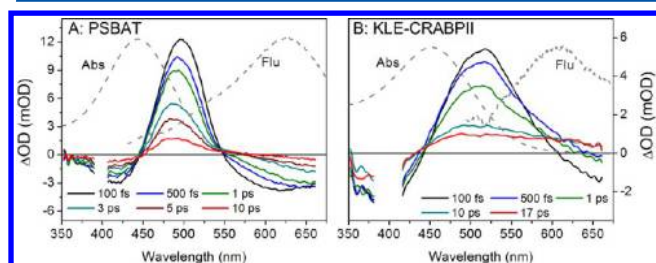
Figure 3. Transient absorption spectra of (A) PSBAT in methanol after 400 nm excitation and (B) PSB-KLE-CRABPII mutant after 400 nm excitation. The spectral regions around 400 nm were removed due to pump scatter contamination. Transient spectra are overlapped with static absorption (dashed gray curves as labeled) and fluorescence spectra (dashed gray curves as labeled).

(Figure 3A) are nearly identical to those previously reported,[18,19,102,103] with a negative ground state bleach (GSB) peaking at 425 nm and a negative stimulated emission (SE) band peaking at 610 nm, which both overlap a positive narrow excited state absorption (ESA) band at 505 nm. The rapid decay of these signals is attributed to the nonadiabatic quenching of the first singlet excited state (S_1) population due to twisting.[18,19,102,103] Concurrent with decay, this is a red-shifting of the SE (from 610 to 650 nm) and a blue-shifting of the ESA (from 505 to 490 nm) that is attributed to vibrational relaxation on the S_1 surface.[18,19,104−106] The PSB-KLE-CRABPII signals (Figure 3B) exhibit qualitatively similar spectroscopic features to the PSBAT signals with clearly

resolvable GSB and ESA bands (although distinctly broader) and a SE that is observed only within the first ∼500 fs after photoexcitation (600−675 nm).

Although both PSBAT in solution and PSB-KLE-CRABPII exhibit similar transient spectra, the quantitative differences of the dynamics between the two samples are clearer in the kinetic traces (Figure 4). While the PSBAT kinetics follow similar
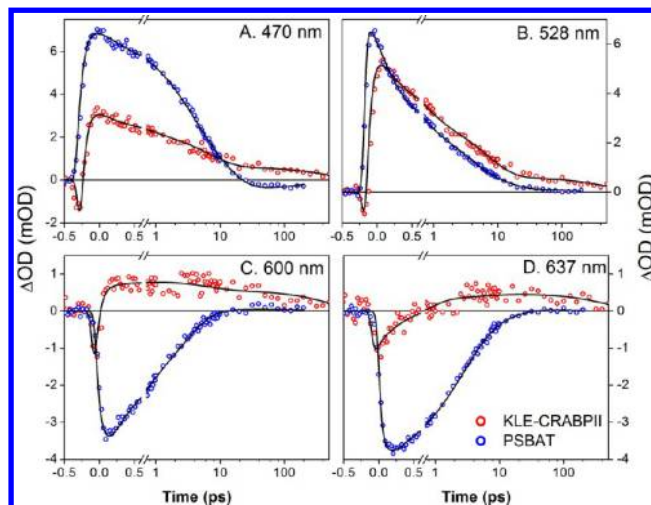
Figure 4. Select transient absorption traces of PSB-KLE-CRABPII in pH 7.2 phosphate buffer (red circles) and PSBAT in methanol (blue circles) overlapping the global analysis fit with sequential model (——) at (A) 470 nm, (B) 528 nm, (C) 600 nm, and (D) 637 nm. Note that the time axis for each panel is linear from −0.5 to 0.5 ps and logarithmic from 1.25 to 200 ps.

decay kinetics across all probe wavelengths, the evolution of the PSB-KLE-CRABPII signals varies strongly with probe wavelength (e.g., the 470 nm kinetics are significantly more slowly evolving than the 528 nm kinetics, which in turn evolves more slowly than the 600 and 637 nm kinetics). The greatest difference between the two samples lies in the low energy region (Figure 4C,D) with the PSB-KLE-CRABPII signals at 600 and 637 nm exhibiting considerably faster sub-ps decay of the SE with the growth of a new positive absorption. To extract a more complete picture of the underlying photodynamics, multiwavelength global analysis is used to simultaneously analyze the signals at all measured probe wavelengths[107,108] and to fit the data into a small number of time-dependent interconnected populations with fixed spectra.

A simple sequential analysis with a linear model (Figure 5A, inset) was used for the PSBAT dynamics to extract the spectra and time scales of constituent populations in the data.[109] Four populations (1−4 in the figure) are resolved, which track the quenching and vibrational relaxation dynamics with the first three populations ascribed to S_1 evolution due to the presence of the SE and a weak final 250 ps component (blue curves) that is ascribed to the primary isomerized *cis* photoproduct. These dynamics can be ascribed to S_1 to ground state (S_0) quenching dynamics with vibrational relaxation (red-shifting SE and blue-shifting ESA) on S_2 as discussed above. In contrast to the PSBAT in solution data, the PSB-KLE-CRABPII dynamics (Figure 5B) requires the use of a more complex nonlinear model that explicitly accounts for the microscopic evolution between coevolving populations. Multiple models were evaluated with the final model providing the best fit to the data within self-consistent constraints (e.g., comparable GSB
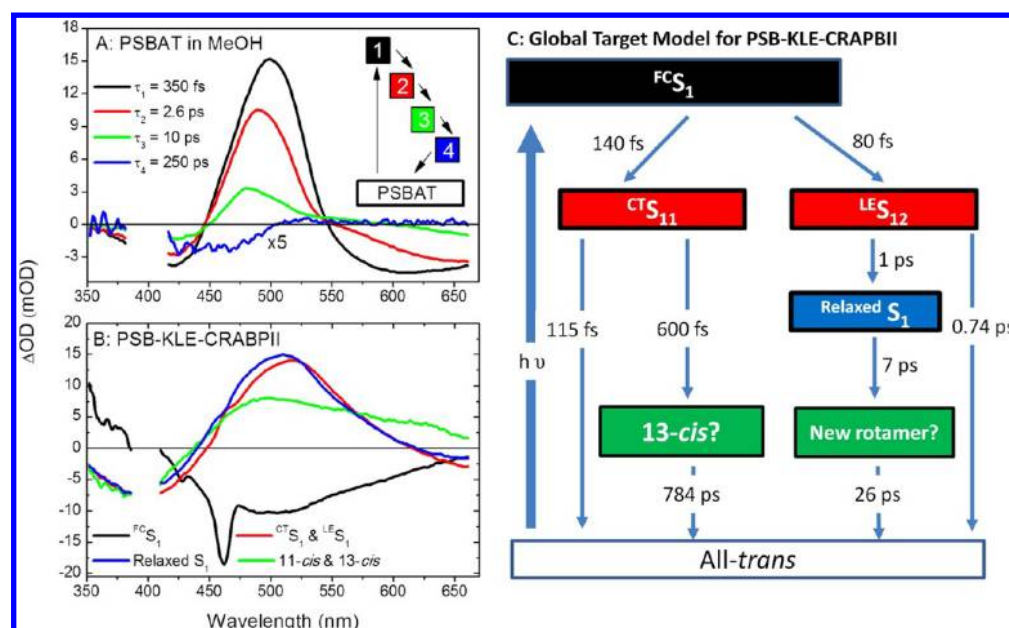
Figure 5. Reconstructed population spectra for (A) PSBAT in methanol via the linear target mode in the inset and (B) PSB-KLE-CRABPII via a target compartmental model. (C) PSB-KLE-CRABPII decay time scales for each component of the model. Model populations and spectra are consistently color coded.

amplitudes). The six-compartment model involves a rapid (<100 fs) bifurcation of the Franck–Condon ($^{FC}S_1$) population into two coexisting "relaxed" S_1 populations ($^{LE}S_1$ and $^{CT}S_1$; the reason behind our use of this nomenclature will be explained later) with identical spectra (red curve). While $^{CT}S_1$ rapidly decays (660 fs) into a red-absorbing S_0 photoproduct (which is tentatively assigned to formation of PSB11 or PSB13, red curve to green curve), $^{LE}S_1$ persists (~8 ps) and exhibits vibrational relaxation (red curve to blue curve) similar to PSBAT in solution. The experiment does not allow for the identification of the photoproduct, but the labeling in Figure 5C is consistent with the mechanistic hypothesis and supporting computational results discussed in section 3.3 below. These results also indicate that $^{LE}S_1$ may decay via an unidentified excited state rotamer (single bond twisting), which is also unidentified in the modeling and eventually relaxes to S_0 reverting back to PSBAT. Unfortunately, this population overlaps strongly with the ESA of the excited state and is poorly spectrally and temporally resolved, so all photoproducts generated from the different excited state pathways are modeled with the same spectrum (green curve).

3.2. Vertical Absorption Energies. The PSB-KLE-CRABPII chromophore has an observed λ^a_{max} of 449 nm.[50,51] The reported λ^a_{max} values of PSBAT and PSB11 in methanol are 445 and 442 nm,[11] respectively. Note that experimental results are only available in methanol, since PSBAT is unstable in water. The λ^a_{max} of PSBAT in methanol is almost identical to that of PSB-KLE-CRABPII, and largely blue-shifted with respect to that of Rh (498 nm).[58] Our first goal was to see if QM/MM models could reproduce the corresponding vertical excitation energy tuning by the protein and solvent environment.

The initial PSB-KLE-CRABPII QM/MM model (i.e., without sampling the environment) yielded λ^a_{max} values of 367 and 372 nm, at CASPT2 and MS-CASPT2 levels, respectively, corresponding to excitation energy errors of 14.2 and 13.2 kcal/mol, respectively, when compared to the

experimental value of 449 nm. This inaccurate result is attributed to a poor modeling of the average location of the highly mobile parts of the protein, especially the complex HBN structure. Therefore, in order to sample the HBN networks, classical MD simulations with a parametrized chromophore (sections 1.c and 1.d in the Supporting Information) were used to obtain different starting solvent configurations. Ten "snapshots" were then obtained from different times from the MD simulation, which were then optimized with CASSCF/AMBER and used for excitation energy calculations. This method gave an average λ^a_{max} value of 400 nm with CASPT2 and 431 nm with MS-CASPT2, corresponding to a 7.8 and 2.7 kcal/mol difference from the observed excitation energy, respectively (Figure 6A). The big difference between the CASPT2 and MS-CASPT2 excitation energies is a consequence of the fact that only the second method allows for state mixing (see section 2.1). However, due to the present MS-CASPT2 formulation, the correct excitation energies would be expected to lie somewhere in between the CASPT2 and MS-CASPT2 values (see the comparison with XMCQDPT2 in section 1.i of the Supporting Information).

The results above indicate that MD sampling is essential for improving the description of the environment around the chromophore in KLE-CRABPII. This is because, in configurationally and conformationally variable systems, the sampling allows us to describe the average effect of the environment which may differ significantly from that of a selected configuration/conformation. In our models, in spite of the improvement with respect to a single configuration, the result of a limited sampling still does not adequately reproduce the experimental data, pointing to the fact that further improvements of the model are required.

While the pK_a of the Schiff base linkage is high in Rh and bR (13.3[110] and 16,[111] respectively), meaning that it is protonated in both proteins, the Schiff base in our mimics has a pK_a of 8.7 and can be either protonated or deprotonated at physiological pH.[51] Therefore, our models should be able to describe both
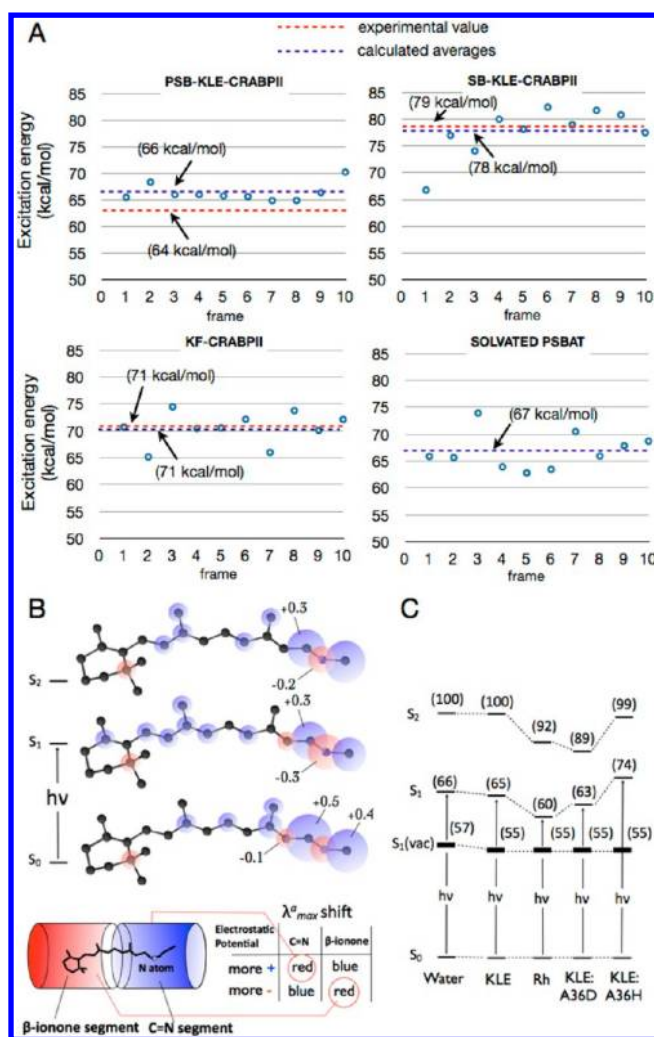
Figure 6. Electronic structure of the ground (S_0), spectroscopic excited state (S_1), and forbidden state (S_2) of the protonated Schiff base of retinal. (A) MS-CASPT2 excitation energies for the CASSCF/AMBER optimized structures obtained starting from 10 MD snapshots. The same data are presented for models containing not only the PSBAT chromophore (PSB-KLE-CRABPII) but also the corresponding unprotonated chromophore (SB-KLE-CRABPII), a mutant containing retinal (KF-CRABPII), and PSBAT in water solution (solvated PSBAT). (B) Top: Change in the charge distribution along the backbone of the isolated chromophore of PSB-KLE-CRABPII upon photoexcitation. The size of each bubble in the diagram reflects the value of the charge on the corresponding center. The numbers in the diagram represent the minimum and maximum values of the Mulliken charges (with hydrogen charges summed together with the heavy atom charges). Bottom: An environment imposing a more positive potential (blue color) on the chromophore C=N segment or a more negative potential on the β-ionone segment (red color) will red-shift the λ^a_{max}. Reversing the displayed electrostatic potential results in a blue-shifted absorption. (C) The effect of the environment on excitation energies is evaluated. The bold lines represent the S_0–S_1 excitation of the extracted chromophores in the gas phase. The solvated PSBAT environment (water) and the PSB-KLE-CRABPII (KLE) environment both have a similar effect, and the shift due to single mutations is evidently due to the electrostatic changes in the environment rather than a change in chromophore geometry.

protonated or deprotonated (SBAT) chromophores correctly. As such, the sampling protocol applied to PSB-KLE-CRABPII, which features a carboxylate and protonated Schiff base forming

an ion pair, was also applied to the SB-KLE-CRABPII and KF-CRABPII (Figure 6A) models featuring a carboxylate polarizing SBAT and a guanidinium group polarizing all-*trans* retinal, respectively. In spite of the chemical diversity of chromophores and environments, the three models reproduce the experimentally observed λ^a_{max} values with similar errors (for calculated energies and oscillator strengths, see sections 3.b and 3.c of the Supporting Information). The chromophore–counterion distances are correlated to the degree of localization of the positive charge in the chromophore. The double bond alternation in the region of the Schiff base (—N=C15—C14=C13—) is different for PSBAT and SBAT, the latter of which exhibits a decreased bond alternation with a longer —N=C15 double bond and a shorter C15—C14 single bond (Figure S5 in the Supporting Information).

For comparison, we provide the results of the sampling for the absorption of PSBAT isolated in water (Figure 6A). We find that the model of PSBAT in solution yields a reasonable excitation energy compared to the experiment if we assume that the water and methanol environments are similar (the excitation energy computed for PSBAT in water is 67 kcal/mol compared to 64.3 kcal/mol in methanol). The similarity of the excitation energy for PSBAT in solution and in KLE-CRABPII (66 kcal/mol) then suggests that the solution and KLE-CRABPII environments have a similar color tuning effect. This is tentatively ascribed to the possibility that the solvent incorporated in the KLE-CRABPII chromophore cavity plays a dominant role in tuning the excitation energy (i.e., by creating a solvent-like microenvironment). Indeed, KLE-CRABPII has a cavity that allows a large number of solvent molecules to surround the chromophore, unlike Rh, whose chromophore cavity only hosts two[3] or three[57] water molecules. Note that this solvent-like environment is found in KLE-CRABPII but may not be found in other CRABPII mutants. Indeed, mutants of a similar rhodopsin mimic, based on the human cellular retinol binding protein II, have been engineered with λ^a_{max} values ranging from 425 to 644 nm.[39]

To gain further understanding of factors affecting the spectroscopy of these systems, the effect of the protein/solvent environments on the λ^a_{max} value of PSBAT has been investigated in each system studied. One frame featuring a λ^a_{max} close to the average value (and assumed to represent the average structure) was selected for each set of data. Single point MS-CASPT2/6-31G* calculations were then carried out for the corresponding isolated chromophores, extracted from their respective optimized protein/solvent structures, to determine their "intrinsic" excitation energies. The results are almost uniformly around 55 kcal/mol difference between S_0 and S_1 (Figure 6C), suggesting that the λ^a_{max} between these proteins is not modulated by the geometry in these cases (see below) but rather by the electrostatic fields imposed on the chromophore π-electron distribution. Indeed, as shown in Figure 7, the chromophore structures of PSB-KLE-CRABPII and PSBAT in solution are very similar and both feature small torsional deformations and a large 45° twist of the β-ionone ring. The chromophore in Rh has similar bond lengths but different dihedrals. It seems that the net effect of the deformation is similar in all three systems, because in the visual pigment the β-ionone ring is ca. −50° twisted and therefore breaks the continuity of the π-system in a similar fashion to PSB-KLE-CRABPII and solvated PSBAT. Notice that the twisting of the C6—C7 bond (i.e., the twisting of the β-ionone ring with respect to the main conjugated chain) has the same effect in
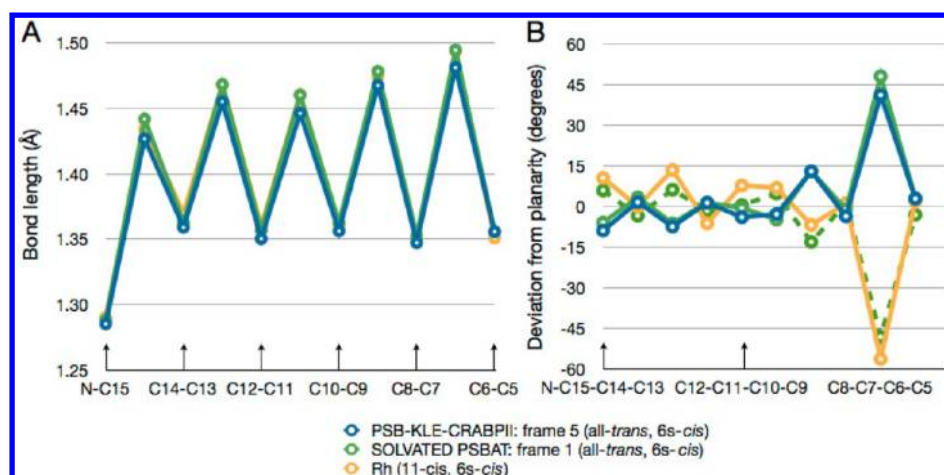
Figure 7. A comparison of the S_0 optimized geometry of PSBAT in solution and protein environment. The geometry of PSBAT in Rh is included for reference. The representative geometries of PSBAT in PSB-KLE-CRABPII and in water solution were taken from the optimized frames 5 and 1 of Figure 6A, respectively. These were determined to be representative frames due to the values of their λ^a_{max} that, as shown in the figure, reproduce the average λ^a_{max} value. (A) Bond length alternation along the chromophore backbone. (B) Deviation from planarity in degrees (with respect to 180 or 0°) of the dihedral angles. The values connected by a dashed line correspond to the mirror image (enantiomer) of the chromophore that is present in solution.
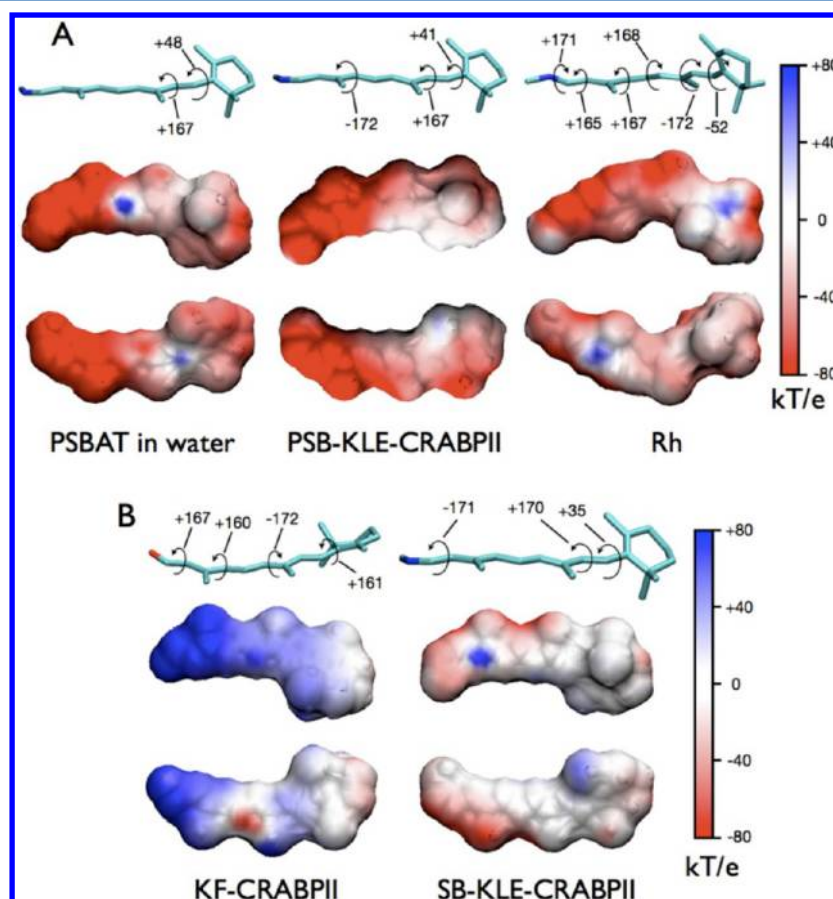
Figure 8. Electrostatic potential map (due to the environment) onto the van der Waals surface of the retinal chromophore surface. The accompanying scales numerically correlate the color to the calculated electrostatic potential, in units of kT/e. Significant torsional distortions are indicated for each chromophore. The backbone dihedral angle values display deformations that deviate from planarity (0 or 180°) by more than 5°. (A) Maps projected onto the positively charged chromophores of PSB-KLE-CRABII, Rh, and PSBAT in water. (B) Maps projected onto the neutral chromophores in KF-CRABPII and SB-KLE-CRABPII.

both PSB11 and PSBAT and is substantially independent of the stereochemistry of the C11═C12 bond. This is consistent with the comparison of Rh to the mirror-image structure of PSBAT

in solution that shows a considerable overlap of geometries (Figure 7B, dashed green curve). For Rh, our conclusion that the geometry of the chromophore in the protein has a small

effect on color tuning conflicts with the conclusions of Bravaya et al.[57] In their study, a third water molecule was added to the model near the protonated Schiff base. It formed a hydrogen bond that caused a torsional distortion of 48° in C13=C14—C15=N which in turn had a significant effect on the calculated excitation energy. Our model included only the two waters seen in the crystal structure and, as a result, had only a 15° distortion in the C13=C14—C15=N dihedral (Figure 8A).

The blue-shifting effect of the environment on vertical excitation energies can be understood on the basis of the charge distributions of the electronic structures of the S_0, S_1, and S_2 states in PSBAT (Figure 6B). Although the charge distributions of the S_0 and S_2 states are similar, the charge distribution of the charge-transfer (S_1) state is marked by a translocation of the positive charge from the —C15=NH— Schiff base region toward the β-ionone ring. As shown in Figure 6C, our calculations indicate that the environments of the Rh, PSB-KLE-CRABPII, and solvent cavities blue-shift the λ^a_{max} values of the corresponding chromophores with respect to the gas phase. Furthermore, inspection of the data reveals the following: (i) This effect is only 5 kcal/mol in Rh. This relatively small change is interpreted in terms of a "counterion quenching" effect which refers to the fact that the large blue-shift induced by the counterion in the chromophore absorption is counterbalanced by a red-shift induced by the rest of the protein residues.[62] However, it has to be pointed out that in a previous Rh model by Andruniow et al.[62] we found an effect even smaller than 5 kcal/mol. This is explained by the differences between the present Rh model and the Andruniow et al. model (e.g., the use of the 1U19 instead of the 1HZX crystallographic structures), indicating that the exact magnitude of the counterion quenching depends on how the model has been constructed.[74,75,112,113] Also, notice that the documented counterion quenching refers to Rh (i.e., bovine rhodopsin) and shall not be generalized to all rhodopsins, which feature λ^a_{max} values ranging from 350 to 630 nm.[4,5] (ii) The blue-shift induced by both the KLE-CRABPII cavity and solvent cavity is larger than the one computed for the Rh cavity. In KLE-CRABPII, this is ascribed to the presence of a carboxylate counterion whose effect is not counterbalanced by the rest of the protein residues. In fact, as explained above, this system displays a solvent-like microenvironment where the solvent is screening the effect of the protein residues but not the effect of the counterion. Notice that, as previously reported,[114−117] in the solvent environment the effect of the counterion is replaced by a cluster of solvent molecules with their negative poles (e.g., oxygens in H_2O and MeOH) oriented toward the positively charged Schiff base group. This also results in a shielding of the real counterion (e.g., Cl−) called the "leveling effect".[118]

The effects described above can be easily visualized and quantitatively studied by mapping the electrostatic potential imposed by the protein pocket on the van der Waals surface of the chromophore (Figure 8). In all cases, the environment blue-shifting effect is due to a negative potential projected on the positive —C15=NH— Schiff base charge (red region). The maps can also explain the red-shift observed in Rh relative to the PSB-KLE-CRABPII and solvated models. The excitation energy of Rh is 6.3 kcal/mol red-shifted from PSB-KLE-CRABPII due to the weaker negative electrostatic potential projected on the protonated Schiff base region of the chromophore in Rh and the increased negative potential around the C7 and C8 atoms near the β-ionone ring (Figure 8A) which partially counterbalances the effect of the counterion

Systems containing neutral chromophores have more positive charge projected along the complete chromophore (Figure 8B); it is likely that the water molecules near the chromophore in SB-KLE-CRABPII orient differently than in PSB-KLE-CRABPII because of the absence of a positive charge. As a result, the water molecules cause the SB-KLE-CRABPII excitation energy (364 nm) to be identical to the λ^a_{max} of SBAT in methanol solution.[11] On the other hand, the strong positive potential at the aldehyde functional group in KF-CRABPII is caused by the proximal positively charged R111 residue that is not present in the other mutants. In the case of the unbound all-*trans* retinal, excitation to the S_1 state initiates charge transfer and a negative charge shifts to the oxygen of the aldehyde. As with both PSBAT and SBAT, a positive electrostatic potential from the environment near the aldehyde functional will red-shift the λ^a_{max} of an unbound chromophore. That is what is observed both computationally and experimentally in the case of KF-CRABPII and explains why the KF-CRABPII is red-shifted relative to the unprotonated SB-KLE-CRABPII system.

It follows from these conclusions that point mutations of nearby residues can modify the electrostatic potentials, leading to alterations of the λ^a_{max} values (Figure 6B). To quantify the extent of this effect, we computed the structure of new PSB-KLE-CRABPII mutants featuring a charged residue replacing the A36 residue located near a poorly solvated region of PSBAT. In our model, this residue has a significant potential to modulate λ^a_{max} because it is relatively isolated from the solvent and is in proximity to C7 and C8 (near the β-ionone ring). Using an average representative structure (frame 3) of the PSB-KLE-CRABPII system, two new mutants were created *in silico*: A36D with a negatively charged aspartate and A36H with a positively charged histidine. The electrostatic potential argument predicts that the A36D and A36H mutants would have red-shifted and blue-shifted λ^a_{max} values, respectively. Indeed, a 2.1 kcal/mol red-shift was computed for A36D and a 6.7 kcal/mol blue-shift for A36H, which is consistent with the color regulation mechanism described above. These predicted effects shall be considered upper limits, as no HBN sampling was performed on the two mutants. Indeed, internal water redistribution may lead to partial solvation of the ionized residues with a consequent decrease in their electrostatic effect. Furthermore, a change in the conformation of the nearby side chains and even protein backbone may occur, but these factors are beyond the scope of this section, which aims only to investigate whether the same color-tuning mechanism found in other rhodopsins also applies to CRABPII-based rhodopsin mimics.

3.3. Vertical Emission Energies. As discussed in section 3.1, the S_1 state of PSB-KLE-CRABPII displays (experimentally) a spectroscopy and photophysics close to that observed for PSBAT in solution. The data indicate that, in polar solvents (e.g., methanol), PSBAT relaxes via two non-interconverting channels, which correspond to reactive and nonreactive pathways with respect to generating isomerized photoproducts.[103,105] The reactive population, after the initial relaxation, follows a path similar to the one documented for the visual receptor Rh[119] and leads to double bond isomerization; the nature of the second nonreactive channel is still unclear. However, both the reactive and nonreactive channels form on a <50 fs time scale after photon absorption, leading to a stimulated emission maximum centered around 700 nm,[103] close to the observed stationary 675 nm λ^f_{max} value.[120] As shown in Figure 5C in PSB-KLE-CRABPII, two species
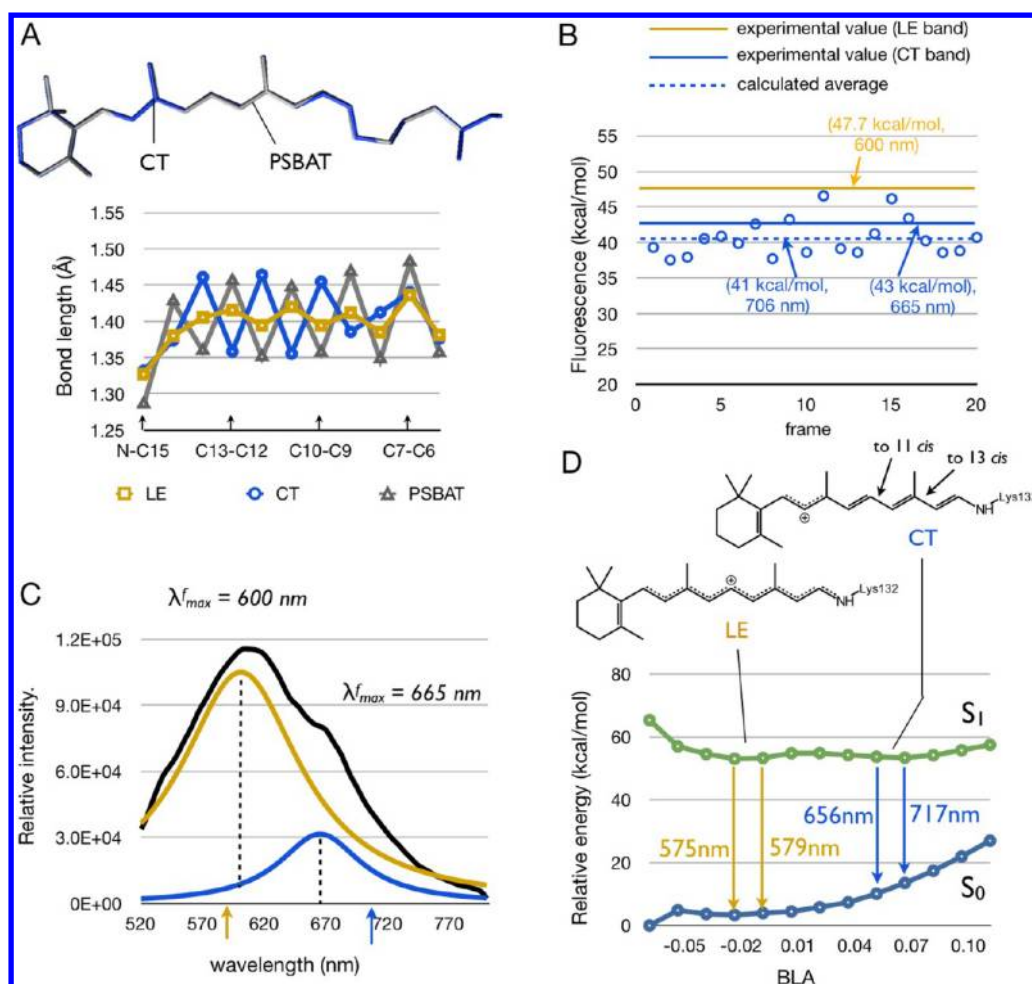
Figure 9. Fluorescent states of PSB-KLE-CRABPII. (A) BLA patterns for the S_0 optimized structure (gray triangles), as well as both LE-like (yellow squares) and CT-like (blue circles) populations of S_1 optimized structures. The LE population has low ("even") BLA, while the CT population has inverted BLA. As shown in the top superposition between representative S_0 (PSBAT) and S_1 (CT) structures, there is very limited change in the torsional deformation occurring upon S_1 optimization. (B) As the BLA of the excited state becomes more inverted, the fluorescence becomes more red-shifted. The CASPT2 vertical excitation energies describing the emission of 20 S_1 optimized structures are shown here. The average value falls within 2.5 kcal/mol of the experimentally observed peak that is hypothesized to correspond to the CT population. (C) Fluorescent spectrum of PSBAT in the protein environment obtained by subtracting the fluorescence spectrum of KLE-CRABII from the fluorescence spectrum of PSB-KLE-CRABPII. (D) Limit resonance structures representing the "even" population (LE) and the "inverted" population (CT) of part A. The arrows indicate the potentially isomerizing double bonds in positions 11 and 13. The results of a CASPT2 scan along the BLA coordinate indicate that there are two minima that correspond to the LE and CT BLA patterns. Numeric values for BLA are the average value of double bond length minus single bond length, in Å. λ^f_{max} values are calculated as 575 and 717 nm from the two minima, but calculated fluorescence wavelengths from neighboring points that are nearly degenerate to the minima on the S_1 surface are included to give a more thorough description of the fluorescence region. The first point is with ground state optimized geometry, and its energy is used as a reference.

(indicated as $^{CT}S_1$ and $^{LE}S_1$) appear within 150 fs and are tentatively associated with the same reactive and nonreactive species observed in methanol. In the following, this assignment will be discussed on the basis of a computational investigation of the S_1 potential energy surface.

In order to simulate the fluorescence (process b in Figure 2), the average "relaxed" S_1 structure(s) must be determined. To determine the nature of the S_1 species and take into account the PSBAT and HBN structural variability, a short (ca. 50 fs) QM/MM trajectory was computed to describe the fast initial S_1 relaxation of PSB-KLE-CRABPII and starting from frame 3 in Figure 6A. Only the PSBAT and waters were allowed to relax (to sample the HBN network), while the protein was held fixed. Rapid oscillations in the bond length alternation (BLA; defined as the difference between the average double bond and average single bond lengths) of S_1 PSBAT were observed during the

simulation, indicating that the structural changes mainly involve stretching modes. The BLA associated with the two extremes of the oscillation are markedly different, with the first exhibiting an almost "even" BLA pattern featuring single and double bonds having similar bond lengths (the BLA value is close to zero); the other extreme is a highly "inverted" BLA pattern (Figures 9A and S6 of the Supporting Information depict these geometries, and the coordinates are presented in sections 2.f and 2.g of the Supporting Information). In order to look for possible S_1 minima featuring different BLA patterns, two trajectory snapshots displaying extreme BLA values were used as starting points for classical MD simulations to sample the HBN structure (as done above for the absorption maxima). For each MD computation, 10 evenly spaced snapshots were selected for subsequent QM/MM geometry optimizations. The resulting 20 S_1 equilibrium structures produced, exclusively,
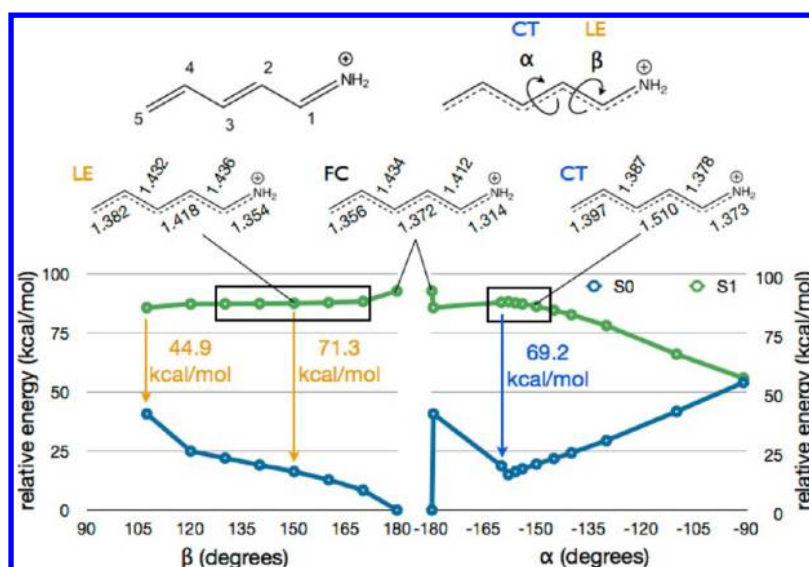
Figure 10. A CASPT2 relaxed scan in PSB3 on S_1 revealed two flat energy regions (see squared frames) with an energy change of <0.5 kcal/mol. One region has a BLA indicative of an LE population, and the other, a BLA consistent with a CT population. The LE population relaxes by twisting around a single bond (dihedral angle β), and the CT state, by twisting around the central double bond (dihedral angle α). The results of CASPT2 relaxed scans along these twisting coordinates are shown. The irregular shape of the relaxed scan at low values of α is due to the isomerization of PSB3 along β, which leads to a a reduced S_0–S_1 energy gap (the structure at around α = 180 has β =107, corresponding to the S_1 minimum observed along the β scan).

structures with an inverted BLA value and yielded an average vertical excitation energy of 41 kcal/mol (706 nm). This number has to be compared with the observed emission λ^f_{max} values (see below). As would be expected with the inverted BLA, all structures feature a positive charge translocated toward the β-ionone ring and therefore are part of a charge-transfer (CT) population. The original central double bonds (e.g., C11═C12 and C13═C14) now have single bond orders and can twist easily. These excited state minima are therefore associated with a reactive (with respect to double bond isomerization, see section 3.4) $^{CT}S_1$ species.

The experimental fluorescence spectrum, however, has a shoulder that suggests the presence of two bands (Figure 9C). A two-peak deconvolution performed with PeakFit (section 3.e in the Supporting Information) resolves two bands centered at 600 and 665 nm (Figure 9C) that were associated with the $^{CT}S_1$ and $^{LE}S_1$ populations, respectively, and were presented in the ultrafast data in Figure 5. The 665 nm maximum is associated with the computed 704 nm λ^f_{max} value. The reactive population $^{CT}S_1$ would therefore correlate with a CT population characterized by an inverted BLA. The second 600 nm maximum would correspond to the alternative $^{LE}S_1$ nonreactive population, but the CASSCF/AMBER calculations were not able to locate the corresponding equilibrium structure on the S_1 potential energy surface.

The fact that CASSCF/AMBER optimizations starting from 20 MD snapshots with very different BLA values all produced S_1 structures with similar BLA patterns could be due to the fact that CASSCF does not include dynamic electron correlation, thus failing to locate alternative S_1 minima. For this reason, we evaluated the CASPT2 energy profile along a CASSCF/AMBER "relaxed" scan starting from 1 of the 20 optimized structures (point 4 in Figure 9B was selected because its energy is closest to the average energy) and moving along points with decreasing BLA values (i.e., points displaying single and double bond lengths yielding BLA values getting closer to that of the S_0 equilibrium structure). As the results in Figure 9D show, this

energy profile indicates the existence of a S_1 potential energy surface with two flat minima. While the first minimum corresponds to the CT structure described above (excitation energies in the 656−717 range), the second features a locally excited (LE) structure characterized by an even BLA in the central part of the molecule and by a positive charge delocalized on the same fragment. The LE structure is energetically located slightly below the CT structure, with a computed emissive energy gap in the 575−579 nm range that falls close to the primary fluorescence band λ^f_{max} at 600 nm (Figure 9C). A stabilization of LE structures upon inclusion of the dynamic correlation is supported by reported CASPT2 geometry optimizations on computationally affordable reduced retinal chromophore models[121] and in a recent QM/MM study of 11-cis locked bovine Rh.[35] These studies demonstrate the existence of an energy minimum displaying an even BLA in the central part of the molecule.

Due to the far too high cost of CASPT2 optimizations, the CASPT2 BLA scan of Figure 9D was performed on geometries optimized with a CASSCF-based methodology. As a consequence, the flat LE minimum needs further investigation. To address this problem, the PSB3 (see section 2.1) reduced model of PSBAT was used to study the S_1 potential energy surface, and to provide further support for the existence of the two excited state species. PSB3 exhibits similar excited state behavior to PSBAT and allows for the use of CASPT2 geometry optimization due to its smaller size (Figure 10). LE and CT flat regions were indeed found on the S_1 energy surface. Due to its double bond/single bond inversion, the CT structure can readily isomerize. In fact, the twisting deformation about the central C2═C3 double bond (see angle α in Figure 10) produces a short flat S_1 region that gives access to a lower lying conical intersection between the S_1 and S_0 potential energy surfaces. The LE structure, on the other hand, is located at the center of a flat S_1 region mainly spanned by the twisting deformation about a single C1—C2 bond (see angle β in Figure 10). Therefore, the evolution of LE does not seem to
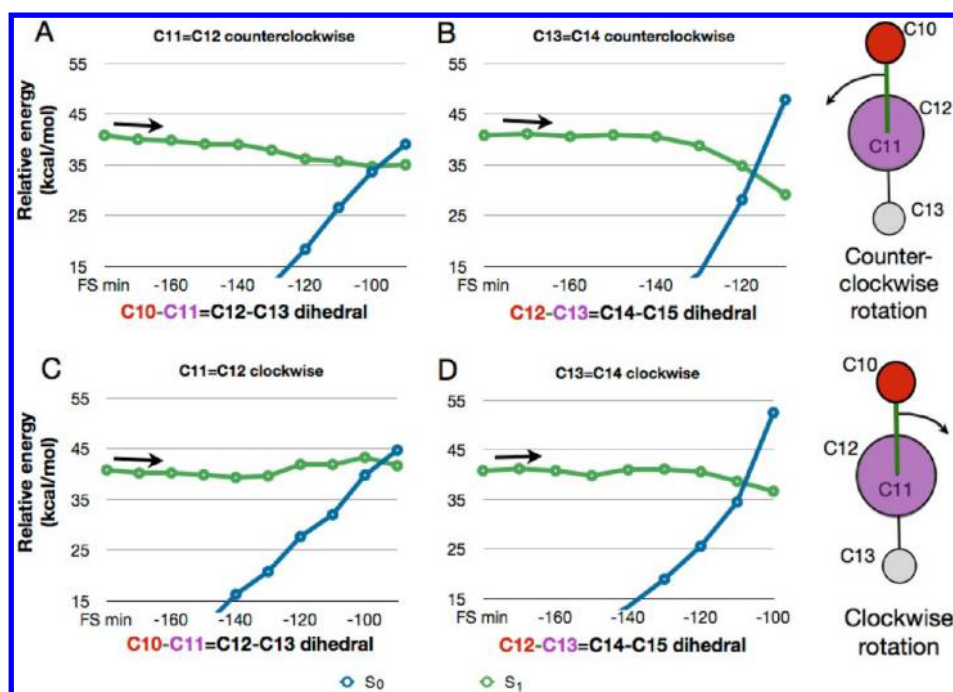
Figure 11. Results of the relaxed scans of PSB-KLE-CRABPII, starting from the CT minimum, showing energies corrected by second order perturbation theory at the CASPT2//CASSCF/AMBER level, all relative to the S_0 energy at CT. Parts A and B are scans of isomerizations in the counterclockwise direction, and have no potential energy barrier, while parts C and D are in the clockwise direction and have barriers of 3.9 and 1.3 kcal/mol, respectively. Arrows are guides to the eye of evolution direction.

lead to an isomerization product but to a lower energy conformer with a ca. 105° twisted single bond.

The LE and CT species proposed above will display different photophysics, possibly producing a dual-fluorescence signal if they slowly interconvert (with respect to the fluorescence lifetime). This hypothesis seems to be consistent with the assignment of CT and LE to the observed $^{CT}S_1$ and $^{LE}S_1$ populations, respectively. This possibility is also consistent with recent computational[122] and experimental[123] reports looking at the excited state behavior of PSBAT in methanol, which argue for the existence of two different S_1 populations with different spectral and temporal properties. One state was assigned to a nonreactive S_1 intermediate (not leading to isomerization) with a 2.8 ps lifetime in methanol and the other to a reactive intermediate with a lifetime of 5.2 ps. In addition, averaged solvent electrostatic potential/molecular dynamics (ASEP/MD) computations (a QM/MM approach that uses a mean field approximation) at the CASPT2//CASSCF level of a PSBAT model in methanol support the possibility of dual fluorescence in these systems.[124] The fluorescent species would have, according to the authors, CT character and covalent/diradical character due to near degeneracy and crossing of the S_1 and S_2 potential energy surfaces that display different electronic structures. However, to explain a dual fluorescence, these species should both have high oscillator strength and the S_2 state must thus have a mixed character supposedly close to the one indicated as a LE state in the present contribution.

3.4. Excited State Evolution. Both the transient dynamics of PSBAT in solution[123] and the PSB-KLE-CRABPII signals (see section 3.1) indicate that photoproducts are generated upon S_1 decay. To determine which bond could potentially isomerize in the PSB-KLE-CRABPII pocket, relaxed S_1 scans along both C10—C11=C12—C13 and C12—C13=C14—C15 dihedrals were computed starting at the CT minimum of

Figure 9D (corresponding to point 4 in Figure 9B) where the central double bonds have single bond character and are prepared for isomerization. No relaxed scans have been computed for the LE pathway.

In Figure 11, we present results of four scans computed in different directions (clockwise or anticlockwise) along two different dihedral angles (around C11=C12 or C13=C14). An S_0 and S_1 degeneracy was reached corresponding to a conical intersection after as little as 60° rotation for the C13=C14 twisting (Figure 11B), consistent with what has been reported for bR and ASR models,[31,67] or after as much as 90° rotation for the C11=C12 twisting, consistent with what has been reported for Rh.[78,122]

Three of the four scans indicate that the S_1 population is driven toward a conical intersection leading to rapid decay to S_0. Indeed, counterclockwise rotation around either C11=C12 and C13=C14 and clockwise rotation around C13=C14 occurs along a flat potential energy surface with less than 1.5 kcal/mol barriers. In contrast, the clockwise rotation around C11=C12 has a ca. 4 kcal/mol barrier and should be, according to our results, less competitive. The origin of this barrier is ascribed to the steric interactions of P39 with the chromophore's methyl group that swings out to within 2.27 Å of the P39 side chain at a 90° twisted geometry (Figure S9, Supporting Information). The fact that the scans indicate only one possible direction of rotation for formation of the PSB11 product and two possible directions of rotation for formation of PSB13 product from the CT minimum supports the tentative photoproduct assignments in Figure 5.

The results above indicate that the S_1 population may decay via different reactive processes (C11=C12 and C13=C14 twisting) controlled by small barriers located along flat potential energy surface regions. These processes would limit the S_1 lifetime and the fluorescence efficiency (e.g., process b in
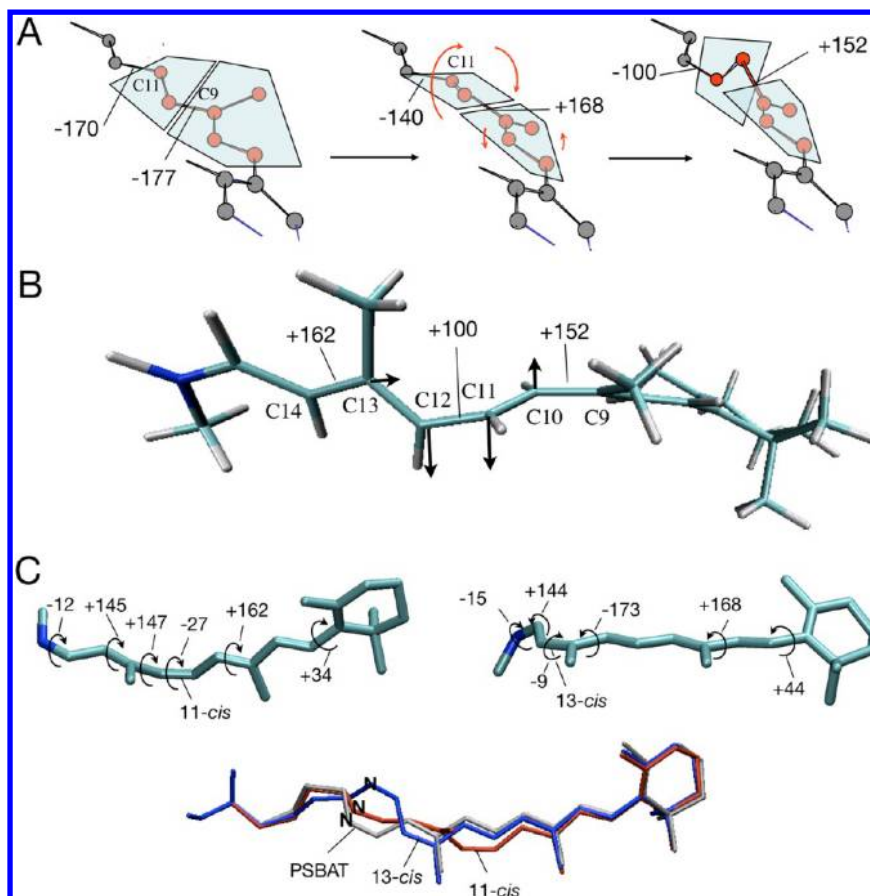
Figure 12. The counterclockwise motion of PSB-KLE-CRABPII during its isomerization observed from the relaxed scan around C11=C12 is a bicycle pedal motion. (A) The C7=C8—C9=C10 and C9=C10—C11=C12 dihedrals remain mostly planar, while rotation occurs around the C9=C10 bond, and to a lesser extent around the C7=C8 bond, which can both be classified as single bonds in the CT state. The degree labels are the deviations from planarity of the isomerizing C11=C12 bond, and of the C9=C10 bond, whose rotation defines the bicycle pedal behavior. (B) The motions of the carbon atoms during the isomerization are depicted. While in Rh, C12 was observed to be a motionless pivot point,[116] in PSB-KLE-CRABPII, C12 moves in tandem with C11 and the motion of C10 is slightly diminished. (C) Structures and main dihedral angles (deg) for the computed 11-*cis* (left) and 13-*cis* (right) primary photoproducts. The backbone dihedral values display deformations that deviate from planarity (0 or 180°) of more than 5°. At the bottom, we report the superposition of PSBAT in PSB-KLE-CRABPII and the corresponding isomerized chromophores.

Figure 2). However, notice that the approximations made do not presently allow the correct magnitude of the barrier to be determined (which is expected to be at most on the order of a few kcal/mol), whether rotation around C11=C12 or C13=C14 is preferred or if the following decay leads to an observable photoproduct. Also, the decay of the LE population is not investigated here. This may result in a twisted conformer (i.e., about a single bond) of the excited state chromophore (contributing to the fluorescence with a hypothetically further red-shifted emission with respect to the ones reported in Figure 9C and consistent with the PSB3 model of Figure 10). For the moment, this remains a speculation that may be the target of future investigations.

The computed counterclockwise PSBAT to PSB11 isomerization mechanism in PSB-KLE-CRABPII is similar to that resolved for Rh (PSB11 to PSBAT).[78,122] In both cases, a space-saving asynchronous bicycle pedal motion[125−127] occurred, whereby the rotation of C10—C11=C12—C13 is accompanied by the partial torsional rotation around *both* neighboring double bonds (C9=C10 and C13=C14) that also acquire single bond character in S_1 (see Figure 12A and B for the process corresponding to Figure 11A). Notice that, similar to Rh, the +152° C9=C10 dihedral must revert back, as

expected for an aborted bicycle pedal motion.[126] This is demonstrated by the computed structure of the photoproduct (see below) where the same angle has a larger +162° value (see Figure 12C, top left). In contrast, the PSBAT to PSB13 isomerization in KLE-CRABPII is best compared to ASR where a similar isomerization process occurs. In ASR, a bicycle pedal coordinate involving the C15=N bond has been documented.[31] In KLE-CRABPII, the motion around C15=N reaches a −26° torsional deformation and then reverses direction after C13=C14 has reached −100° and returns toward the original angle (−2°) at the photoproduct geometry (−15°) (see also section 4.b in the Supporting Information).

3.5. Photoproducts. The PSB11 and PSB13 photoproducts were modeled assuming that the protein remains substantially unchanged so that only the HBN and isomerized chromophore are relaxed during the calculation. Accordingly, the last structures of the counterclockwise 11-*cis* and 13-*cis* scans (Figure 11A and B, respectively) were relaxed on S_0 to generate the PSB11 and PSB13 equilibrium structures (Figure 12C, top). The PSB13 product was found to be 4.3 kcal/mol more stable than the PSB11 product at the CASPT2 level.

The photoproduct λ^a_{max} values were calculated at the CASPT2 level to be at 466 and 492 nm for PSB11 and

PSB13, respectively. These transitions are 5 and 8 kcal/mol red-shifted from the calculated 431 nm λ^a_{max} of the PSB-KLE-CRABPII reactant, respectively. Since the protein pocket of CRABPII is adapted to bind the PSBAT chromophore (i.e., all-*trans* isomer), the isomerized products are presumably unstable at room temperature and hence would revert back to the original structure. Indeed, the optimized geometries of PSB11 and PSB13 are significantly distorted, with dihedrals −27 and −9° twisted out of plane, respectively. These deformations extend to other parts of the chromophore backbone. In fact, from Figure 12C (bottom), it can be seen that the isomerization leads, in both cases, to large skeletal changes that mainly involve the N-containing segment of the chromophore, while the segment starting at C9 and comprising the β-ionone ring seems to undergo a limited displacement. This happens even though the β-ionone ring sticks out of the protein pocket and would be, in principle, allowed to rotate.

4. CONCLUSIONS

We have constructed tentative QM/MM models for a set of CRABPII-based rhodopsin mimics. It is shown that the presence of many solvent molecules in the protein cavity of the mimics makes the modeling difficult and decreases its accuracy. This suggests that, in spite of the reported improvement upon a limited MD sampling, further effort has to be made to consistently model artificial and natural rhodopsins mainly but not exclusively, due to the need to properly describe the loosely bound solvent molecules in the protein cavity. This may be achieved by more sampling (e.g., longer dynamics with more snapshots) or by improving the quality of the sampling (e.g., sampling a larger part of the system by relaxing cavity side chains).

The λ^a_{max} and geometries of the chromophore in solution have been found to be similar to those of the chromophore bound in KLE-CRABPII. Also, time-resolved spectroscopy of PSB-KLE-CRABPII reveals different time scales that, similar to what has been documented for PSBAT in solution,[123] are assigned to formation and decay (via internal conversion and photoisomerization) of two independent or slowly interconverting S_1 species. The similarity of the spectroscopy, geometry, and excited state reactivity of PSBAT in the solvent and in KLE-CRABPII suggests that KLE-CRABPII offers a solvent-like microenvironment, at least more so than in typical rhodopsins like Rh.

The weak stationary fluorescence observed for PSB-KLE-CRABPII could be studied by sampling the S_1 potential energy surface via a short excited state QM/MM trajectory. In line with the result of time-resolved spectroscopy, the computations indicate that the observed emission band contains the contribution of two S_1 species whose relative stability could not be established. One species (LE) has a delocalized charge and could only be located along a CASPT2 energy profile. The other species (CT) features a charge located close to the β-ionone ring and shows an inverted BLA pattern. Counter-clockwise scans around C11=C12 and C13=C14 starting from the CT species point to facile isomerizations. However, since no persistent S_0 photoproducts are observed in the PSB-KLE-CRABPII samples or revealed by transient absorption spectra, the computed PSB11 and PSB13 equilibrium structures must necessarily correspond to unstable intermediates.

The results revised above support the use of QM/MM models for the *in silico* screening of spectral and reactivity properties of CRABPII-based rhodopsin mimics as well as of

their mutants. It is hoped that further work in this area could lead to valuable tools for the systematic design and production of genetically encodable probes or light-responsive actuators with desired properties. However, this seems to primarily require an improved sampling of the complex HBN which links the internal solvent molecules with the cavity residues. Accordingly, a longer sampling which also involves the cavity side chains is likely to represent the initial direction for future work on this topic.

■ ASSOCIATED CONTENT

ⓢ Supporting Information

Methodological details (Figures S1−S4 and Tables S1−S4). Cartesian coordinates of the optimized structures. Energy and oscillator strength values (Figures S5 and S6 and Tables S5−S10). Relaxed scans (Figures S7−S10). Experimental details (Figure S11). This material is available free of charge via the Internet at http://pubs.acs.org.

■ AUTHOR INFORMATION

Corresponding Author

*E-mail: dlarsen@ucdavis.edu (D.S.L.); molivuc@bgsu.edu (M.O.). Phone: 530-754-9075 (D.S.L.); 419-372-7606 (M.O.).
Notes
The authors declare no competing financial interest.

■ ACKNOWLEDGMENTS

■ REFERENCES

(1) Spudich, J. L.; Yang, C. S.; Jung, K. H.; Spudich, E. N. Retinylidene Proteins: Structures and Functions from Archaea to Humans. *Annu. Rev. Cell Dev. Biol.* **2000**, 16, 365−392.

(2) Van der Horst, M. A.; Hellingwerf, K. J. Photoreceptor Proteins, "Star Actors of Modern Times": A Review of the Functional Dynamics in the Structure of Representative Members of Six Different Photoreceptor Families. *Acc. Chem. Res.* **2004**, 37, 13−20.

(3) Okada, T.; Sugihara, M.; Bondar, A. N.; Elstner, M.; Entel, P.; Buss, V. The Retinal Conformation and Its Environment in Rhodopsin in Light of a New 2.2 Angstrom Crystal Structure. *J. Mol. Biol.* **2004**, 342, 571−583.

(4) Kleinschmidt, J.; Harosi, F. I. Anion Sensitivity and Spectral Tuning of Cone Visual Pigments Insitu. *Proc. Natl. Acad. Sci. U.S.A.* **1992**, 89, 9181−9185.

(5) Yokoyama, S. Molecular Evolution of Vertebrate Visual Pigments. *Prog. Retinal Eye Res.* **2000**, 19, 385−419.

(6) Yokoyama, S.; Yokoyama, R. Adaptive Evolution of Photoreceptors and Visual Pigments in Vertebrates. *Annu. Rev. Ecol. Syst.* **1996**, 27, 543−567.

(7) Makino, C. L.; Groesbeek, M.; Lugtenburg, J.; Baylor, D. A. Spectral Tuning in Salamander Visual Pigments Studied with Dihydroretinal Chromophores. *Biophys. J.* **1999**, *77*, 1024−1035.

(8) Wood, P.; Partridge, J. C. Opsin Substitution Induced in Retinal Rods of the Eel (Anguilla Anguilla (L.)): A Model for G-Protein-Linked Receptors. *Proc. R. Soc. B* **1993**, *254*, 227−232.

(9) Booth, P. J.; Farooq, A. Intermediates in the Assembly of Bacteriorhodopsin Investigated by Time-Resolved Absorption Spectroscopy. *Eur. J. Biochem.* **1997**, *246*, 674−680.

(10) Dimitrov, D.; He, Y.; Mutoh, H.; Baker, B. J.; Cohen, L.; Akemann, W.; Knöpfel, T. Engineering and Characterization of An Enhanced Fluorescent Protein Voltage Sensor. *PLoS One* **2007**, *2e*, 440.

(11) Freedman, K. A.; Becker, R. S. Comparative Investigation of the Photoisomerization of the Protonated and Unprotonated Normal-Butylamine Schiff-Bases of 9-cis-Retinals, 11-cis-retinals, 13-cis-retinals, and All-trans-retinals. *J. Am. Chem. Soc.* **1986**, *108*, 1245−1251.

(12) Koyama, Y.; Kubo, K.; Komori, M.; Yasuda, H.; Mukai, Y. Effect of Protonation on the Isomerization Properties of Normal-Butylamine Schiff-Base of Isomeric Retinal as Revealed by Direct HPLC Analyses-Selectino of Isomerization Pathways by Retinal Proteins. *Photochem. Photobiol.* **1991**, *54*, 433−443.

(13) Doig, S. J.; Reid, P. J.; Mathies, R. A. Picosecond Time-Resolved Resonance Raman-Spectroscopy of Bacteriorhodopsin-J, Bacterlorhodopsin-K, Bacterlorhodopsin-Kl Intermediates. *J. Phys. Chem.* **1991**, *95*, 6372−6379.

(14) Mathies, R. A.; Cruz, C. H. B.; Pollard, W. T.; Shank, C. V. Diresct Observation of the Femtosecond Excited-State Cis-Trans Isomerization in Bacteriorhodopsin. *Science* **1988**, *240*, 777−779.

(15) Rohr, M.; Gartner, W.; Schweitzer, G.; Holzwarth, A. R.; Braslavsky, S. E. Quantum Yields of the Photochromic Equilibrium Between Bacteriorhodopsin and Its Bathointermediate-K - Femtosecond and Nanosecond Optoacoustic Spectroscopy. *J. Phys. Chem.* **1992**, *96*, 6055−6061.

(16) Varo, G. Analogies between Halorhodopsin and Bacteriorhodopsin. *Biochim. Biophys. Acta* **2000**, *1460*, 220−229.

(17) Schoenlein, R. W.; Peteanu, L. A.; Mathies, R. A.; Shank, C. V. The 1st Step in Vision - Femtosecond Isomerization of Rhodopsin. *Science* **1991**, *254*, 412−415.

(18) Hamm, P.; Zurek, M.; Roschinger, T.; Patzelt, H.; Oesterhelt, D.; Zinth, W. Femtosecond Spectroscopy of the Photoisomerisation of the Protonated Schiff Base of All-trans Retinal. *Chem. Phys. Lett.* **1996**, *263*, 613−621.

(19) Logunov, S. L.; Song, L.; ElSayed, M. A. Excited-state Dynamics of a Protonated Retinal Schiff Base in Solution. *J. Phys. Chem.* **1996**, *100*, 18586−18591.

(20) Bates, M.; Huang, B.; Zhuang, X. Super-Resolution Microscopy by Nanoscale Localization of Photo-Switchable Fluorescent Probes. *Curr. Opin. Chem. Biol.* **2008**, *12*, 505−514.

(21) Day, R. N.; Davidson, M. W. The Fluorescent Protein Palette: Tools for Cellular Imaging. *Chem. Soc. Rev.* **2009**, *38*, 2887−2921.

(22) Meyer, A. J.; Dick, T. P. Fluorescent Protein-Based Redox Probes. *Antioxid. Redox Signaling* **2010**, *13*, 621−650.

(23) Narita, A.; Ogawa, K.; Sando, S.; Aoyama, Y. Visible Sensing of Nucleic Acid Sequences Using a Genetically Encodable Unmodified MRNA Probe. *Nucleic Acids Symp. Ser.* **2006**, 283−284.

(24) Newman, R. H.; Fosbrink, M. D.; Zhang, J. Genetically Encodable Fluorescent Biosensors for Tracking Signaling Dynamics in Living Cells. *Chem. Rev.* **2011**, *111*, 3414−3466.

(25) Schifferer, M.; Griesbeck, O. Application of Aptamers and Autofluorescent Proteins for RNA Visualization. *Integr. Biol.* **2009**, *1*, 499−505.

(26) Shank, N. I.; Zanotti, K. J.; Lanni, F.; Berget, P. B.; Armitage, B. A. Enhanced Photostability of Genetically Encodable Fluoromodules Based on Fluorogenic Cyanine Dyes and a Promiscuous Protein Partner. *J. Am. Chem. Soc.* **2009**, *131*, 12960−12969.

(27) Berthold, P.; Tsunoda, S. P.; Ernst, O. P.; Mages, W.; Gradmann, D.; Hegemann, P. Channelrhodopsin-1 Initiates Photo-taxis and Photophobic Responses in Chlamydomonas by Immediate Light-Induced Depolarization. *Plant Cell* **2008**, *20*, 1665−1677.

(28) Kianianmomeni, A.; Stehfest, K.; Nematollahi, G.; Hegemann, P.; Hallmann, A. Channelrhodopsins of Volvox Carteri Are Photochromic Proteins That Are Specifically Expressed in Somatic Cells under Control of Light, Temperature, and the Sex Inducer. *Plant Physiol.* **2009**, *151*, 347−366.

(29) Paternolli, C.; Neebe, M.; Stura, E.; Barbieri, F.; Ghisellini, P.; Hampp, N.; Nicolini, C. Photoreversibility and Photostability in Films of Octopus Rhodopsin Isolated from Octopus Photoreceptor Membranes. *J. Biomed. Mater. Res.* **2009**, *88A*, 947−951.

(30) Kawanabe, A.; Furutani, Y.; Jung, K. H.; Kandori, H. Photochromism of Anabaena Sensory Rhodopsin. *J. Am. Chem. Soc.* **2007**, *129*, 8644−8649.

(31) Strambi, A.; Durbeej, B.; Ferré, N.; Olivucci, M. Anabaena Sensory Rhodopsin Is a Light-Driven Unidirectional Rotor. *Proc. Natl. Acad. Sci. U.S.A.* **2010**, *107*, 21322−21326.

(32) Hampp, N. A. Bacteriorhodopsin: Mutating a Biomaterial into an Optoelectronic Material. *Appl. Microbiol. Biotechnol.* **2000**, *53*, 633−639.

(33) Lindvold, L. R.; Ramanujam, P. S. The Use of Bacteriorhodopsin in Optical Processing - a Review. *J. Sci. Ind. Res.* **1995**, *54*, 55−66.

(34) Kandori, H.; Matuoka, S.; Shichida, Y.; Yoshizawa, T.; Ito, M.; Tsukida, K.; Baloghnair, V.; Nakanishi, K. Mechanism of Isomerization of Rhodopsin Studied by Use of 11-cis-Locked Rhodopsin Analogues Excited with a Picosecond Laser Pulse. *Biochemistry* **1989**, *28*, 6460−6467.

(35) Laricheva, E. N.; Gozem, S.; Rinaldi, S.; Melaccio, F.; Valentini, A.; Olivucci, M. Origin of Fluorescence in 11-cis Locked Bovine Rhodopsin. *J. Chem. Theory Comput.* **2012**, *8*, 2559−2563.

(36) Kralj, J. M.; Hochbaum, D. R.; Douglass, A. D.; Cohen, A. E. Electrical Spiking in Escherichia coli Probed with a Fluorescent Voltage-Indicating Protein. *Science* **2011**, *333*, 345−348.

(37) Kralj, J. M.; Douglass, A. D.; Hochbaum, D. R.; Maclaurin, D.; Cohen, A. E. Optical Recording of Action Potentials in Mammalian Neurons Using a Microbial Rhodopsin. *Nat. Methods* **2012**, *9*, 90−U130.

(38) Lee, K. S. S.; Berbasova, T.; Vasileiou, C.; Jia, X.; Wang, W.; Choi, Y.; Nossoni, F.; Geiger, J. H.; Borhan, B. Probing Wavelength Regulation with an Engineered Rhodopsin Mimic and a C15-Retinal Analogue. *ChemPlusChem* **2012**, *77*, 273−276.

(39) Wang, W.; Nossoni, Z.; Berbasova, T.; Watson, C. T.; Yapici, I.; Lee, K. S.; Vasileiou, C.; Geiger, J. H.; Borhan, B. Tuning the Electronic Absorption of Protein-Embedded All-trans-Retinal. *Science* **2012**, *338*, 1340−1343.

(40) Shaw, W. V. Protein Engineering. The Design, Synthesis and Characterization of Factitious Proteins. *Biochem. J.* **1987**, *246*, 1−17.

(41) Heim, R.; Prasher, D. C.; Tsien, R. Y. Wavelength Mutations and Posttranslational Autoxidation of Green Fluorescent Protein. *Proc. Natl. Acad. Sci. U.S.A.* **1994**, *91*, 12501−12504.

(42) Razeghifard, R.; Wallace, B. B.; Pace, R. J.; Wydrzynski, T. Creating Functional Artificial Proteins. *Curr. Protein Pept. Sci.* **2007**, *8*, 3−18.

(43) Khoury, G. A.; Fazelinia, H.; Chin, J. W.; Pantazes, R. J.; Cirino, P. C.; Maranas, C. D. Computational Design of Candida Boidinii Xylose Reductase for Altered Cofactor Specificity. *Protein Sci.* **2009**, *18*, 2125−2138.

(44) Kent, K. P.; Oltrogge, L. M.; Boxer, S. G. Synthetic Control of Green Fluorescent Protein. *J. Am. Chem. Soc.* **2009**, *131*, 15988−15989.

(45) Wiedenmann, J.; Ivanchenko, S.; Oswald, F.; Schmitt, F.; Rocker, C.; Salih, A.; Spindler, K. D.; Nienhaus, G. U. EosFP, a Fluorescent Marker Protein with UV-Inducible Green-to-Red Fluorescence Conversion. *Proc. Natl. Acad. Sci. U.S.A.* **2004**, *101*, 15905−15910.

(46) Dahiyat, B. I.; Mayo, S. L. De Novo Protein Design: Fully Automated Sequence Selection. *Science* **1997**, *278*, 82−87.

(47) Jiang, L.; Althoff, E. A.; Clemente, F. R.; Doyle, L.; Rothlisberger, D.; Zanghellini, A.; Gallaher, J. L.; Betker, J. L.;

Tanaka, F.; Barbas, C. F. I.; et al. De Novo Computational Design of Retro-Aldol Enzymes. *Science* **2008**, *319*, 1387−1391.

(48) Jin, W. Z.; Kambara, O.; Sasakawa, H.; Tamura, A.; Takada, S. De Novo Design of Foldable Proteins with Smooth Folding Funnel: Automated Negative Design and Experimental Verification. *Structure* **2003**, *11*, 581−590.

(49) Watanabe, H. C.; Mori, Y.; Tada, T.; Yokoyama, S.; Yamato, T. Molecular Mechanism of Long-Range Synergetic Color Tuning between Multiple Amino Acid Residues in Conger Rhodopsin. *Biophysics* **2010**, *6*, 67−68.

(50) Crist, R. M.; Vasileiou, C.; Rabago-Smith, M.; Geiger, J. H.; Borhan, B. Engineering a Rhodopsin Protein Mimic. *J. Am. Chem. Soc.* **2006**, *128*, 4522−4523.

(51) Vasileiou, C.; Vaezeslami, S.; Crist, R. M.; Rabago-Smith, M.; Geiger, J. H.; Borhan, B. Protein Design: Reengineering Cellular Retinoic Acid Binding Protein II into a Rhodopsin Protein Mimic. *J. Am. Chem. Soc.* **2007**, *129*, 6140−6148.

(52) Bolen, D. W.; Rose, G. D. Structure and Energetics of the Hydrogen-Bonded Backbone in Protein Folding. *Annu. Rev. Biochem.* **2008**, *77*, 339−362.

(53) Boylan, J. F.; Gudas, L. J. Overexpression of the Cellular Retinoic Acid Binding Protein-i (Crabp-I) Results in a Reduction in Differentiation-Specific Gene-Expression in F9 Teratocarcinoma Cells. *J. Cell Biol.* **1991**, *112*, 965−979.

(54) Gaub, M. P.; Lutz, Y.; Ghyselinck, N. B.; Scheuer, I.; Pfister, V.; Chambon, P.; Rochette-Egly, C. Nuclear Detection of Cellular Retinoic Acid Binding Proteins I and II with New Antibodies. *J. Histochem. Cytochem.* **1998**, *46*, 1103−1111.

(55) Napoli, J. L. Retinoic Acid Biosynthesis and Metabolism. *FASEB. J.* **1996**, *10*, 993−1001.

(56) Vaezeslami, S.; Jia, X. F.; Vasileiou, C.; Borhan, B.; Geiger, J. H. Structural Analysis of Site-Directed Mutants of Cellular Retinoic Acid-Binding Protein II Addresses the Relationship between Structural Integrity and Ligand Binding. *Acta Crystallogr., Sect. D* **2008**, *64*, 1228−1239.

(57) Bravaya, K. B.; Bochenkova, A.; Granovsky, A.; Nemukhin, A. An Opsin Shift in Rhodopsin: Retinal S0-S1 Excitation in Protein, in Solution, and in the Gas Phase. *J. Am. Chem. Soc.* **2007**, *129*, 13035−13042.

(58) Hurley, J. B.; Ebrey, T. G.; Honig, B.; Ottolenghi, M. Temperature and Wavelength Effects on the Photochemistry of Rhodopsin, Isorhodopsin, Bacteriorhodopsin and Their Photo-products. *Nature* **1977**, *270*, 540−542.

(59) Warshel, A.; Levitt, M. Theoretical Studies of Enzymic Reactions- Dielectric, Electrostatic and Steric Stabilization of Carbonium-Ion in Reaction of Lysozyme. *J. Mol. Biol.* **1976**, *103*, 227−249.

(60) Andersson, K.; Malmqvist, P. A.; Roos, B. O.; Sadlej, A. J.; Wolinski, K. 2nd Order Perturbation Theory with a CASSCF Reference Function. *J. Phys. Chem. B* **1990**, *94*, 5483−5488.

(61) Finley, J.; Malmqvist, P. A.; Roos, B. O.; Serrano-Andres, L. The Multi-State CASPT2Method. *Chem. Phys. Lett.* **1998**, *288*, 299−306.

(62) Andruniow, T.; Ferré, N.; Olivucci, M. Structure, Initial Excited-State Relaxation, and Energy Storage of Rhodopsin Resolved at the Multiconfigurational Perturbation Theory Level. *Proc. Natl. Acad. Sci. U.S.A.* **2004**, *101*, 17908−17913.

(63) Coto, P. B.; Marti, S.; Oliva, M.; Olivucci, M.; Merchan, M.; Andres, J. Origin of the Absorption Maxima of the Photoactive Yellow Protein Resolved via Ab Initio Multiconfigurational Methods. *J. Phys. Chem. B* **2008**, *112*, 7153−7156.

(64) Coto, P. B.; Strambi, A.; Ferré, N.; Olivucci, M. The Color of Rhodopsins at the Ab Initio Multiconfigurational Perturbation Theory Resolution. *Proc. Natl. Acad. Sci. U.S.A.* **2006**, *103*, 17154−17159.

(65) Pistolesi, S.; Sinicropi, A.; Pogni, R.; Basosi, R.; Ferré, N.; Olivucci, M. Modeling the Fluorescence of Protein-Embedded Tryptophans with Ab Initio Multiconfigurational Quantum Chemistry: The Limiting Cases of Parvalbumin and Monellin. *J. Phys. Chem. B* **2009**, *113*, 16082−16090.

(66) Sinicropi, A.; Andruniow, T.; Ferré, N.; Basosi, R.; Olivucci, M. Properties of the Emitting State of the Green Fluorescent Protein Resolved at the CASPT2//CASSCF/CHARMM Level. *J. Am. Chem. Soc.* **2005**, *127*, 11534−11535.

(67) Strambi, A.; Coto, P. B.; Ferré, N.; Olivucci, M. Effects of Water Re-Location and Cavity Trimming on the CASPT2//CASSCF/AMBER Excitation Energy of Rhodopsin. *Theor. Chem. Acc.* **2007**, *118*, 185−191.

(68) Strambi, A.; Coto, P. B.; Frutos, L. M.; Ferré, N.; Olivucci, M. Relationship between the Excited State Relaxation Paths of Rhodopsin and Isorhodopsin. *J. Am. Chem. Soc.* **2008**, *130*, 3382−3388.

(69) Altun, A.; Yokoyama, S.; Morokuma, K. Quantum Mechanical/Molecular Mechanical Studies on Spectral Tuning Mechanisms of Visual Pigments and Other Photoactive Proteins. *Photochem. Photobiol.* **2008**, *84*, 845−854.

(70) Altoè, P.; Cembran, A.; Olivucci, M.; Garavelli, M. Aborted Double Bicycle-Pedal Isomerization with Hydrogen Bond Breaking Is the Primary Event of Bacteriorhodopsin Proton Pumping. *Proc. Natl. Acad. Sci. U.S.A.* **2010**, *107*, 20172−20177.

(71) Andruniow, T.; Ferré, N.; Olivucci, M. Structure, Initial Excited-State Relaxation, and Energy Storage of Rhodopsin Resolved at the Multiconfigurational Perturbation Theory Level. *Proc. Natl. Acad. Sci. U.S.A.* **2004**, *101*, 17908−17913.

(72) Ferré, N.; Olivucci, M. Probing the Rhodopsin Cavity with Reduced Retinal Models at the CASPT2//CASSCF/AMBER Level of Theory. *J. Am. Chem. Soc.* **2003**, *125*, 6868−6869.

(73) Munoz-Losa, A.; Galvan, I. F.; Aguilar, M. A.; Martin, M. E. Retinal Models: Comparison of Electronic Absorption Spectra in the Gas Phase and in Methanol Solution. *J. Phys. Chem. B* **2008**, *112*, 8815−8823.

(74) Tomasello, G.; Olaso-Gonzalez, G.; Altoe, P.; Stenta, M.; Serrano-Andres, L.; Merchan, M.; Orlandi, G.; Bottoni, A.; Garavelli, M. Electrostatic Control of the Photoisomerization Efficiency and Optical Properties in Visual Pigments: On the Role of Counterion Quenching. *J. Am. Chem. Soc.* **2009**, *131*, 5172−5186.

(75) Fujimoto, K.; Hayashi, S.; Hasegawa, J.; Nakatsuji, H. Theoretical Studies on the Color-Tuning Mechanism in Retinal Proteins. *J. Chem. Theory Comput.* **2007**, *3*, 605−618.

(76) Hoffmann, M.; Wanko, M.; Strodel, P.; Konig, P. H.; Frauenheim, T.; Schulten, K.; Thiel, W.; Tajkhorshid, E.; Elstner, M. Color Tuning in Rhodopsins: The Mechanism for the Spectral Shift between Bacteriorhodopsin and Sensory Rhodopsin II. *J. Am. Chem. Soc.* **2006**, *128*, 10808−10818.

(77) Fantacci, S.; Migani, A.; Olivucci, M. CASPT2//CASSCF and TDDFT//CASSCF Mapping of the Excited State Isomerization Path of a Minimal Model of the Retinal Chromophore. *J. Phys. Chem. A* **2004**, *108*, 1208−1213.

(78) Frutos, L. M.; Andruniow, T.; Santoro, F.; Ferré, N.; Olivucci, M. Tracking the Excited-State Time Evolution of the Visual Pigment with Multiconfigurational Quantum Chemistry. *Proc. Natl. Acad. Sci. U.S.A.* **2007**, *104*, 7764−7769.

(79) Olivucci, M., Ed. *Computational Photochemistry*; Elsevier Science: Boston, MA, 2005.

(80) Valsson, O.; Angeli, C.; Filippi, C. Excitation Energies of Retinal Chromophores: Critical Role of the Structural Model. *Phys. Chem. Chem. Phys.* **2012**, *14*, 11015−11020.

(81) Gozem, S.; Huntress, M.; Schapiro, I.; Lindh, R.; Granovsky, A. A.; Angeli, C.; Olivucci, M. Dynamic Electron Correlation Effects on the Ground State Potential Energy Surface of a Retinal Chromophore Model. *J. Chem. Theory Comput.* **2012**, *8*, 4069−4080.

(82) Altun, A.; Yokoyama, S.; Morokuma, K. Mechanism of Spectral Tuning Going from Retinal in Vacuo to Bovine Rhodopsin and Its Mutants: Multireference Ab Initio Quantum Mechanics/Molecular Mechanics Studies. *J. Phys. Chem. B* **2008**, *112*, 16883−16890.

(83) Coccia, E.; Varsano, D.; Guidoni, L. Protein Field Effect on the Dark State of 11-cis Retinal in Rhodopsin by Quantum Monte Carlo/Molecular Mechanics. *J. Chem. Theory Comput.* **2012**, *9*, 8−12.

(84) Phillips, J. C.; Braun, R.; Wang, W.; Gumbart, J.; Tajkhorshid, E.; Villa, E.; Chipot, C.; Skeel, R. D.; Kale, L.; Schulten, K. Scalable Molecular Dynamics with NAMD. *J. Comput. Chem.* **2005**, *26*, 1781−1802.

(85) Duan, Y.; Wu, C.; Chowdhury, S.; Lee, M. C.; Xiong, G. M.; Zhang, W.; Yang, R.; Cieplak, P.; Luo, R.; Lee, T.; et al. A Point-Charge Force Field for Molecular Mechanics Simulations of Proteins Based on Condensed-Phase Quantum Mechanical Calculations. *J. Comput. Chem.* 2003, 24, 1999–2012.

(86) Aquilante, F.; De Vico, L.; Ferré, N.; Ghigo, G.; Malmqvist, P.-A.; Neogrády, P.; Pedersen, T. B.; Pitonák, M.; Reiher, M.; Roos, B. O.; et al. MOLCAS 7: The Next Generation. *J. Comput. Chem.* 2010, 31, 224–247.

(87) Granovsky, A. A. Extended Multi-Configuration Quasi-Degenerate Perturbation Theory: The New Approach to Multi-State Multi-Reference Perturbation Theory. *J. Chem. Phys.* 2011, 134, 214113.

(88) Granovsky, A. A. http://classic.chem.msu.su/gran/firefly/index.html.

(89) Bravaya, K. B.; Bochenkova, A. V.; Granovsky, A. A.; Savitsky, A. P.; Nemukhin, A. V. Modeling Photoabsorption of the AsFP595 Chromophore. *J. Phys. Chem. A* 2008, 112, 8804–8810.

(90) Bravaya, K. B.; Bochenkova, A. V.; Granovskii, A. A.; Nemukhin, A. V. Modeling of the Structure and Electronic Spectra of Green Fluorescent Protein Chromophore. *Russ. J. Phys. Chem. B* 2008, 2, 671–675.

(91) De Vico, L.; Pegado, L.; Heimdal, J.; Soderhjelm, P.; Roos, B. O. The Ozone Ring Closure as a Test for Multi-State Multi-Configurational Second Order Perturbation Theory (MS-CASPT2). *Chem. Phys. Lett.* 2008, 461, 136–141.

(92) Kessel, L.; Nielsen, I. B.; Bochenkova, A. V.; Bravaya, K. B.; Andersen, L. H. Gas-Phase Spectroscopy of Protonated 3-OH Kynurenine and Argpyrimidine. Comparison of Experimental Results to Theoretical Modeling. *J. Phys. Chem. A* 2007, 111, 10537–10543.

(93) Khrenova, M. G.; Bochenkova, A. V.; Nemukhin, A. V. Modeling Reaction Routes from Rhodopsin to Bathorhodopsin. *Proteins* 2010, 78, 614–622.

(94) Nemukhin, A. V.; Bochenkova, A. V.; Bravaya, K. B.; Granovsky, A. A. *Proc. SPIE* 2007, 6449, 64490.

(95) Rocha-Rinza, T.; Christiansen, O.; Rajput, J.; Gopalan, A.; Rahbek, D. B.; Andersen, L. H.; Bochenkova, A. V.; Granovsky, A. A.; Bravaya, K. B.; Nemukhin, A. V.; et al. Gas Phase Absorption Studies of Photoactive Yellow Protein Chromophore Derivatives. *J. Phys. Chem. A* 2009, 113, 9442–9449.

(96) Serrano-Andres, L.; Merchan, M.; Lindh, R. Computation of Conical Intersections by Using Perturbation Techniques. *J. Chem. Phys.* 2005, 122, 104107.

(97) Carroll, E. C.; Compton, O. C.; Madsen, D.; Osterloh, F. E.; Larsen, D. S. Ultrafast Carrier Dynamics in Exfoliated and Functionalized Calcium Niobate Nanosheets in Water and Methanol. *J. Phys. Chem. C* 2008, 112, 2394–2403.

(98) Ekvall, K.; van der Meulen, P.; Dhollande, C.; Berg, L. E.; Pommeret, S.; Naskrecki, R.; Mialocq, J. C. Cross Phase Moculation Artifact in Liquid Phase Transient Absorption Spectroscopy. *J. Appl. Phys.* 2000, 87, 2340–2352.

(99) Lorenc, M.; Ziolek, M.; Naskrecki, R.; Karolczak, J.; Kubicki, J.; Maciejewski, A. Artifacts in Femtosecond Transient Absorption Spectroscopy. *Appl. Phys. B: Lasers Opt.* 2002, 74, 19–27.

(100) Shaw, G. S.; Childs, R. F. Characterization of Retinylidene iminium Salts by High-Field 1H and 13C Nuclear Magnetic Resonance Spectroscopy. In *Methods in Enzymology*; Lester, P., Ed.; Academic Press: New York, 1990; Vol 189, pp 112–122.

(101) Andersen, L. H.; Nielsen, I. B.; Kristensen, M. B.; El Ghazaly, M. O. A.; Haacke, S.; Nielsen, M. B.; Petersen, M. A. Absorption of Schiff-Base Retinal Chromophores in Vacuo. *J. Am. Chem. Soc.* 2005, 127, 12347–12350.

(102) Rajput, J.; Rahbek, D. B.; Andersen, L. H.; Hirshfeld, A.; Sheves, M.; Altoe, P.; Orlandi, G.; Garavelli, M. Probing and Modeling the Absorption of Retinal Protein Chromophores in Vacuo. *Angew. Chem., Int. Ed.* 2010, 49, 1790–1793.

(103) Zgrablic, G.; Haacke, S.; Chergui, M. Heterogeneity and Relaxation Dynamics of the Photoexcited Retinal Schiff Base Cation in Solution. *J. Phys. Chem. B* 2009, 113, 4384–4393.

(104) Schmidt, B.; Sobotta, C.; Heinz, B.; Laimgruber, S.; Braun, M.; Gilch, P. Excited-State Dynamics of Bacteriorhodopsin Probed by Broadband Femtosecond Fluorescence Spectroscopy. *Biochim. Biophys. Acta* 2005, 1706, 165–173.

(105) Zgrablic, G.; Voitchovsky, K.; Kindermann, M.; Haacke, S.; Chergui, M. Ultrafast Excited State Dynamics of the Protonated Schiff Base of All-Trans Retinal in Solvents. *Biophys. J.* 2005, 88, 2779–2788.

(106) Hou, B.; Friedman, N.; Ruhman, S.; Sheves, M.; Ottolenghi, M. Ultrafast Spectroscopy of the Protonated Schiff Bases of Free and C-13=C-14 Locked Retinals. *J. Phys. Chem. B* 2001, 105, 7042–7048.

(107) Holzwarth, A. R. Data Analysis in Time-Resolved Measurements. In *Biophysical Techniques in Photosynthesis*; Amesz, J., Hoff, A. J., Eds.; Kluwer Acadmic Publishers: Dordrecht, The Netherlands, 1996.

(108) van Stokkum, I. H. M.; Larsen, D. S.; van Grondelle, R. Global and Target Analysis of Time-Resolved Spectra. *Biochim. Biophys. Acta* 2004, 1657, 82–104.

(109) van Stokkum, L. H. M.; Lozier, R. H. Traget Analysis of the Bacteriorhodopsin Photocycle Using a Spectrotemporal Model. *J. Phys. Chem. B* 2002, 106, 3477–3485.

(110) Druckmann, S.; Ottolenghi, M.; Pande, A.; Pande, J.; Callender, R. H. Acid-Base-Equilibrium of the Schiff-Base in Bacteriorhodopsin. *Biochemistry* 1982, 21, 4953–4959.

(111) Steinberg, G.; Ottolenghi, M.; Sheves, M. Pk(a) of the Protonated Schiff-Base of Bovine Rhodopsin - a Study with Artificial Pigments. *Biophys. J.* 1993, 64, 1499–1502.

(112) Schreiber, M.; Sugihara, M.; Okada, T.; Buss, V. Quantum Mechanical Studies on the Crystallographic Model of Bathorhodopsin. *Angew. Chem., Int. Ed.* 2006, 45, 4274–4277.

(113) Sekharan, S.; Sugihara, M.; Buss, V. Origin of Spectral Tuning in Rhodopsin - It Is Not the Binding Pocket. *Angew. Chem., Int. Ed.* 2007, 46, 269–271.

(114) Altoè, P.; Stenta, M.; Garavelli, M. *AIP Conf. Proc.* 2007, 963, 689.

(115) Cembran, A.; Bernardi, F.; Olivucci, M.; Garavelli, M. The Retinal Chromophore/Chloride Ion Pair: Structure of the Photo Isomerization Path and Interplay of Charge Transfer and Covalent States. *Proc. Natl. Acad. Sci. U.S.A.* 2005, 102, 6255–6260.

(116) Houjou, H.; Inoue, Y.; Sakurai, M. Physical Origin of the Opsin Shift of Bacteriorhodopsin. Comprehensive Analysis Based on Medium Effect Theory of Absorption Spectra. *J. Am. Chem. Soc.* 1998, 120, 4459–4470.

(117) Warshel, A. Calculations of Chemical Processes in Solutions. *J. Phys. Chem.* 1979, 83, 1640–1652.

(118) Blatz, P. E.; Johnson, R. H.; Mohler, J. H.; Al-Dilaimi, S. K.; Dewhurst, S.; Erickson, J. O. Effect of Solution Environment on the Absorption Maxima of Schiff Bases of Retinal. *Photochem. Photobiol.* 2008, 13, 237–245.

(119) Kandori, H.; Sasabe, H. Excited-State Dynamics of a Protonated Schiff-Base of All-Trans-Retinal in Methanol Probed by Femtosecond Fluorescence Measurement. *Chem. Phys. Lett.* 1993, 216, 126–132.

(120) Bachilo, S. M.; Bondarev, S. L.; Gillbro, T. Fluorescence Properties of Protonated and Unprotonated Schiff Bases of Retinal at Room Temperature. *J. Photochem. Photobiol., B* 1996, 34, 39–46.

(121) Valsson, O.; Filippi, C. Photoisomerization of Model Retinal Chromophores: Insight from Quantum Monte Carlo and Multi-configurational Perturbation Theory. *J. Chem. Theory Comput.* 2010, 6, 1275–1292.

(122) Strambi, A.; Coto, P. B.; Frutos, L. M.; Ferré, N.; Olivucci, M. Relationship between the Excited State Relaxation Paths of Rhodopsin and Isorhodopsin. *J. Am. Chem. Soc.* 2008, 130, 3382–3388.

(123) Zgrablic, G.; Novello, A. M.; Parmigiani, F. Population Branching in the Conical Intersection of the Retinal Chromophore Revealed by Multipulse Ultrafast Optical Spectroscopy. *J. Am. Chem. Soc.* 2012, 134, 955–961.

(124) Munoz-Losa, A.; Elena Martin, M.; Fdez Galvan, I.; Luz Sanchez, M.; Aguilar, M. A. Solvent Effects on the Radiative and Nonradiative Decay of a Model of the Rhodopsin Chromophore. *J. Chem. Theory Comput.* 2011, 7, 4050–4059.

(125) Warshel, A. Bicycle-Pedal Model for First Step in Vision Process. *Nature* **1976**, *260*, 679−683.

(126) Warshel, A.; Barboy, N. Energy Storage and Reaction Pathways in the First Step of the Vision Process. *J. Am. Chem. Soc.* **1982**, *104*, 1469−1476.

(127) Schapiro, I.; Weingart, O.; Buss, V. Bicycle-Pedal Isomerization in a Rhodopsin Chromophore Model. *J. Am. Chem. Soc.* **2008**, *131*, 16−17.

10070

dx.doi.org/10.1021/jp305935t | *J. Phys. Chem. B* 2013, 117, 10053−10070